ARTICLE

Adsorptive Avidity of Prussian blue Polypyrrole Nanocomposite for Elimination of Water Contaminants: a Case study of Malachite Green and Isoniazid

Received 00th January 20xx,
Accepted 00th January 20xx

DOI: 10.1039/x0xx00000x

Tabee Jan,[a] Shabnam Raheem,[a] Aamir Hanif,[b] Gaulthier Rydzek,[c] G.M. Peerzada,[a] Katsuhiko Ariga,[d,e] Jin Shang,[f] Masood Ahmad Rizvi.[a*]

Persistent water contaminants include a variety of substances that evade natural cleaning processes posing severe risks to ecosystems. Their adsorptive elimination is a key approach to safer attenuation. Herein we present the design and development of Prussian Blue incorporated Polypyrrole (PPY/PB) hybrid nanocomposite as a high-performance adsorbent for the elimination of malachite green (M.G), isoniazid (INH) and 4-nitrophenol (4-NP) water contaminants. The nanocomposite synthesis was favored by strong dopant-polymer interactions, leading to a PPY/PB material with enhanced electro-active surface area compared to pristine PPY. The structure-activity response of the nanocomposite for the adsorption of target contaminants was unveiled by evaluating its maximum adsorption capacities under environmentally viable conditions. In-depth analysis and optimization of adsorption influencing factors (pH, temperature, and adsorbent dose) were performed. Using equilibrium studies, kinetic model fitting, aided with FTIR analysis, a multi-step mechanism for the adsorption of target contaminants on the nanocomposite was proposed. Furthermore, the PPY/PB nanocomposite also acts as a catalyst, enabling contaminant elimination following a synergistic scheme that was demonstrated using 4-NP contaminant. The synergetic adsorption and catalytic degradation of 4-NP using PPY/PB as adsorbent and catalyst was demonstrated in the presence of $NaBH_4$ as a reducing agent in absence of light. In summary, this work highlights the targeted design of adsorbent, its optimization for adsorptive avidity, and the synergistic role of adsorption trapping in the catalytic degradation of persistent contaminants.

Introduction

The quality of water resources is at risk with the release of persistent organic contaminants into the aquatic environment.[1] These contaminants are characterized by high stability in water, which allows them to evade natural cleansing processes, and water treatment protocols, leading to their ubiquitous environmental distribution, and even prevalence in municipal water distribution facilities.[2] Owing to non-biodegradability and chances of bio-accumulation, these contaminants pose serious health risks to humans and severe disturbances to aquatic ecosystems. For instance, the effluent discharges of the synthetic dye industry often contain a considerable amount of dyes even after general treatment. With an estimated annual dye production of 7.10^5 tonnes, the associated pollution concerns are significant.[3,4] Among other chemicals, Malachite Green (M.G) is widely used for dyeing cotton, wool, and silk fabrics.[5] However, its runoff in effluent gives an aesthetically unpleasant colour to water and is bio-accumulative, a probable carcinogen, and toxic to aquatic organisms.[6] Similarly, trace quantities of pharmaceuticals, particularly antibiotics from agricultural and livestock wastewater effluents, have been classified as emerging contaminants of major concern.[7] The occurrence of antibiotics in the environment poses serious health risks such as the emergence of antibiotic resistant pathogens that are responsible for an estimated 0.7 million deaths annually.[8,9] Isoniazid (INH) one of the first-line antibiotics for tuberculosis was flagged as one of the persistent organic contaminants of concern in wastewater.[10] Out of the various water treatment strategies, including coagulation, oxidation processes and biological removal, adsorption of contaminants has the advantages to be straightforward and potentially economical. Its efficacy ultimately depends upon the adsorbent design.[11] However, widely reported adsorbents such as activated carbon and other biomass-derived carbonaceous materials require intensive modifications and under-desirable adsorption performance.[12,13] Porous conducting polymers have received increasing attention for adsorption applications due to their facile and scalable production, good surface area, and the possibility of surface and functional group modifications towards

[a] Department of Chemistry, University of Kashmir, Hazratbal, Srinagar, Jammu and Kashmir-190006, India
[b] Interdisciplinary Research Center for Hydrogen and Energy Storage (IRC-HES), King Fahd University of Petroleum & Minerals, Dhahran 31261, Saudi Arabia
[c] Institut Charles Gerhardt, UMR 5253, CNRS/ENSCM/UM, ENSCM, Montpellier cedex F-34295, France
[d] Research Center for Materials Nanoarchitectonics (MANA), National Institute for Materials Science (NIMS), 1-1 Namiki, Tsukuba 305-0044, Ibaraki, Japan
[e] Graduate School of Frontier Sciences, The University of Tokyo, 5-1-5 Kashiwanoha, Kashiwa 277-8561, Chiba, Japan
[f] City University of Hong Kong Shenzhen Research Institute, 8 Yuexing 1st Road, Shenzhen Hi-Tech Industrial Park, Nanshan District, Shenzhen, PR China
*Corresponding Author: masoodku2@gmail.com
Electronic Supplementary Information (ESI) available: TGA, XRD, UV-Vis spectroscopy and adsorption studies. See DOI: 10.1039/x0xx00000x

improved adsorption capacity. Besides adsorption, these materials can promote the degradation of contaminants through a two-step synergistic effect. First, adsorption activates persistent contaminants on the surface of the adsorbent. Then the activated contaminant is mineralized or converted into a harmless form by a catalytic reaction.[14] This can be achieved by fine-tuning the properties of conducting polymers by their composite formation with different classes of transition metal complexes. Such composites enable to complement the properties of porous conducting polymers, leading to improved contaminant degradation performances compared to their pristine analogues.[15] Here, Polypyrrole (PPY) was chosen as a porous conducting polymer as its adsorbents have shown high adsorption capacity and selectivity for a variety of dyes and contaminants due to chemisorption and electrostatic interactions .[16-18] However, the impact of transition metal complex doping on polymers for adsorption applications has been scarcely studied. In continuation of our interests in applications of transition metal complexes,[19-21] especially as dopants in conducting polymer matrix for dielectric properties and water treatment applications,[22, 23] we explore here their structure-activity response for the adsorption of dye and antibiotic contaminants under environmentally viable conditions (pH 7, and 20°C). The systematic adsorption study was also envisaged in the synergistic conversion of toxic nitrophenol (4-NP) to non-toxic aminophenol using $NaBH_4$ as a reducing agent in the absence of light, via combined adsorptive and catalytic steps. Prussian blue (PB) was chosen as the transition metal complex to be incorporated in the composite as it is of low cost, stable charge, crystalline nature, lesser toxicity with good surface characteristics making it a suitable dopant in designing sustainable material for water treatment application. In addition, PB, as an adsorbent, has shown exceptional selectivity for the adsorption of cesium ions. This high selectivity is associated with a PB's cubic framework composed of iron centers bound by cyanide bridges, allowing additional cations to intercalate into the interstitial sites. The structure permits small hydrated cations to penetrate, while larger hydrated ions are obstructed. Research findings have demonstrated that the comparable size of the crystal cage of PB and the hydration radius of Cs ions significantly enhance the attraction of Cs ions to PB.[24] Also PB and its analogues have shown a high affinity towards thallium (Tl).[25]

In this work, PPY/PB nanocomposite was synthesized by a facile oxidative polymerization method using pyrrole monomer and nanosized Prussian blue dopant. The synthesized nanocomposite showed an impressive adsorption capacity for M.G. and INH contaminants with maximum adsorption capacities of 15.75 mg/g and 34 mg/g respectively under environmentally viable conditions (pH 7, and 20°C). The enhancement in adsorption capacity of PPY/PB nanocomposite compared to pristine PPY polymer can be attributed to increased interactions between contaminant adsorbates and hybrid adsorbent. The optimization of adsorption influencing factors like pH, temperature, and adsorbent dose, was attempted for applicability of nanocomposite to a wide range of conditions. Using equilibrium studies, kinetic model fitting, and FTIR analysis, an adsorption mechanism was proposed. Taken together this study envisages the targeted design of benign nanocomposite adsorbents and their optimization towards high adsorptive avidity in the attenuation of persistent contaminants under environmental conditions. Besides, it highlights the complementary role of adsorption in the catalytic elimination of persistent contaminants under adsorption-trapped and catalyst-degraded synergism (Scheme 1).

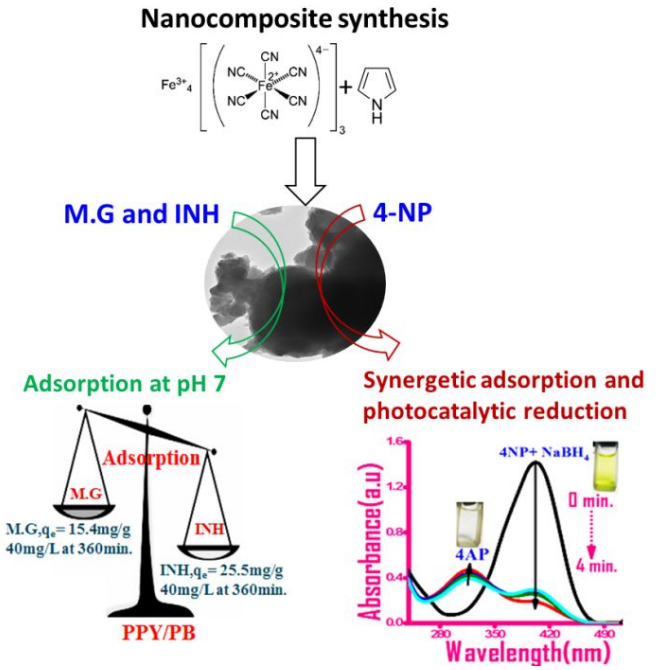

Scheme 1. Schematic depiction of the materials and applications developed in this study.

Results and discussion

Chemical characterization of the PPY/PB nanocomposite

The FT-IR spectra of pure PPY, PB, and PPY/PB nanocomposite are presented in Figure 1(A). The characteristic peaks in the FTIR spectra of PPY are observed at 3411 cm^{-1}, 1553 cm^{-1}, and 1399 cm^{-1} attributed to N-H, C=C, and C-N stretching frequencies of the pyrrole ring, respectively.[26,27] The other vibration bands in the fingerprint region (595-1300 cm^{-1}) can be attributed to N-H, C-H in-plane deformation, and C-H outer bending. The spectrum of PB exhibits vibration bands at around 2080 cm^{-1} and 487 cm^{-1} corresponding to C≡N stretching and Fe(II)-CN-Fe(III) vibrational modes, respectively. Moreover, the broad and low-intensity absorption bands at 3393 cm^{-1} and 1600 cm^{-1} are attributed to O-H stretching and H-O-H bending modes of adsorbed water on the surface of PB.[28] The PPY/PB nanocomposite displays contributions from both PPY and PB with slight shifts, suggesting the successful incorporation of PB dopant into the PPY matrix, most likely by the interaction of dopant PB molecules with PPY's aromatic rings.

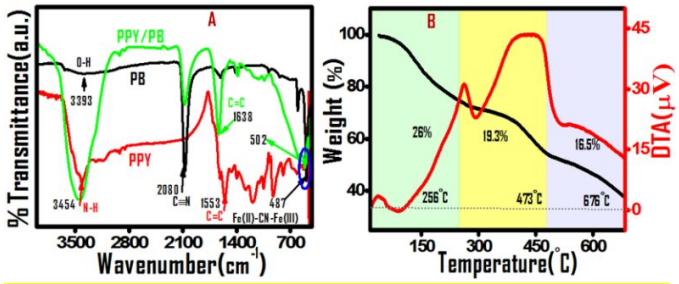

Figure 1. (A) Comparative FTIR spectra of PPY, PB, and the PPY/PB nanocomposite and (B) TGA/DTA analysis of the PPY/PB nanocomposite showing three weight loss steps.

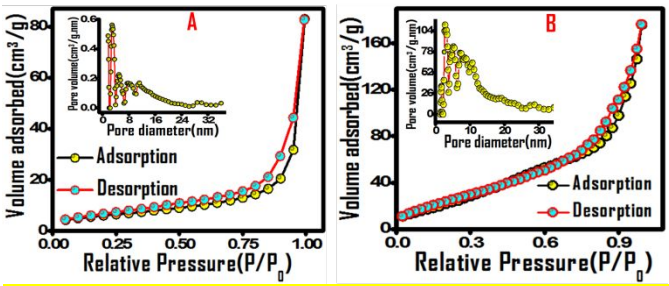

Figure 2. N_2 adsorption-desorption isotherms of (A) PPY and (B) the PPY/PB nanocomposite. Insets depict their corresponding pore size distribution curves.

To confirm these results, the thermal behaviour of the nanocomposite was analyzed by thermogravimetry. TGA/DTA analysis of the PPY/PB nanocomposite is depicted in Figure 1B and that of pristine PPY and PB are shown in Figure S1 (A, B). The observed thermogram of PB shows three weight loss steps characterized by three exothermic peaks at 332°C, 478°C, and 604°C in the DTA curve. The first step is attributed to the removal of absorbed water while the second, with two exothermic peaks, corresponds to the loss of CN moieties. The third transition, with one exothermic dip, is attributed to the decomposition of PB to iron oxide.[29] The TGA curve of pure PPY depicts two transitions, one at a lower temperature up to 94 °C, which can be assigned to the loss of solvent molecules and unreacted monomer. The DTA curve of PPY exhibits an endothermic peak at about 94 °C, indicating that the initial decomposition involves the absorption of heat. The other transition with two exothermic dips starts at around 95°C and ends at 546°C where complete degradation of the PPY chain has occurred. At this temperature, a total weight loss of 50% was reached for the PPY/PB nanocomposite compared to 97% decomposition for the pure PPY. Such an improvement of the thermal stability of the nanocomposite infers stronger interactions after the incorporation of PB dopant into the PPY matrix. The DTA analysis of the nanocomposite exhibits three exothermic peaks, the first two at 258°C and 427°C are due to the elimination of doping ions in PB and PPY, and the third peak at 563°C is due to the decomposition of polymer chains. The synthesised PPY/PB nanocomposite exhibits superior thermal stability compared to that of similar materials reported in the literature. [30,31]

Structural characterization of the PPY/PB nanocomposite

Powder X-ray diffraction was used to identify the crystalline phases and sizes in PPY, PB and in the nanocomposite. The PXRD pattern of PPY shows an amorphous nature with a broad hump at a 2θ value of 25.8° (Figure S2).[32,33] This peak is due to intermolecular pi-pi stacking of pyrrole units.[28,34] The pattern of PB nanoparticles displays well-defined crystalline peaks which can be indexed as the FCC phase with space group Fm3m (No.225) (JCPDS 73-0687) with a lattice parameter of 10.14 Å. From the XRD pattern of PPY/PB, most of the characteristic peaks of PB are present, indicating the incorporation of PB into the polymer matrix. This reveals the successful synthesis of the PPY/PB composite, corroborating the FTIR and TGA analysis. In addition, the observed shifting of PB peaks in the nanocomposite can arise from non-covalent interactions between PPY chains and dopant molecule. These interactions lead to the ordered arrangement of PPY chains within the nanocomposite resulting in higher thermal stability and crystallinity. Meanwhile, compared to the XRD analysis of PB, the degree of crystallinity decreases in the nanocomposite, which is attributed to the amorphous nature of the PPY matrix. Accordingly, crystallite sizes of 29 and 11 nm for PB and PPY/PB were obtained. Next, the surface area of the nanocomposite was investigated by nitrogen sorption. The specific surface area, pore size, and pore volume of an adsorbent are indeed strong influencing parameters that determine adsorption efficiency. The N_2 adsorption/ desorption isotherms of PPY and PPY/PB nanocomposite are given in Figure 2. Both PPY and PPY/PB display a type-IV adsorption isotherm with a hysteresis loop at relatively high pressures, indicating the presence of mesopores as per IUPAC classification.[35-37] Multipoint BET and NLDFT (Non-local Density Functional theory) models were used to calculate the specific surface area and the pore size distribution of the samples. Surface areas of ca 22 m^2/g and 95 m^2/g were obtained for PPY and PPY/PB respectively, with pore volumes of 0.08 cm^3/g and 0.22 cm^3/g. This suggests that the addition of PB nanoparticles to the PPY matrix increases the surface area, due to a higher porosity, which is desirable for an efficient adsorption process. A comparison of the effect of PB dopant on the surface area of PPY composites with other dopants indicates the sizeable enhancement in the surface area of PPY/PB nanocomposite.[38,39] In addition, the pore size diameter (shown in insets of Figure 2) in the materials evolved from mostly mesoporous (2.9 nm) for pure PPY to a mixture of mesopores (2.9 nm) and micropores (<2 nm) for the PPY/PB nanocomposite. Due to its higher surface area, mesoporous structure, and multimodal pore size distribution, PPY/PB can be a potential adsorbent for the attenuation of persistent organic contaminants from aqueous solution. To confirm these results, the morphology and microstructure of PPY, PB, and PPY/PB nanocomposite were examined by using FE-SEM and TEM analysis with the elemental mapping patterns. From the FE-SEM micrographs, the PB dopant exhibited a spherical shaped morphology (Figure 3 (A)) while pristine PPY appears as sheets (zoomed region, Figure 3 (B)). Observations of the PPY/PB composite revealed a uniform dispersion of PB over the PPY surface with a particle diameter of 47nm (Figure 3 (C and D)). Moreover, many cavities get developed in the composite wich may be

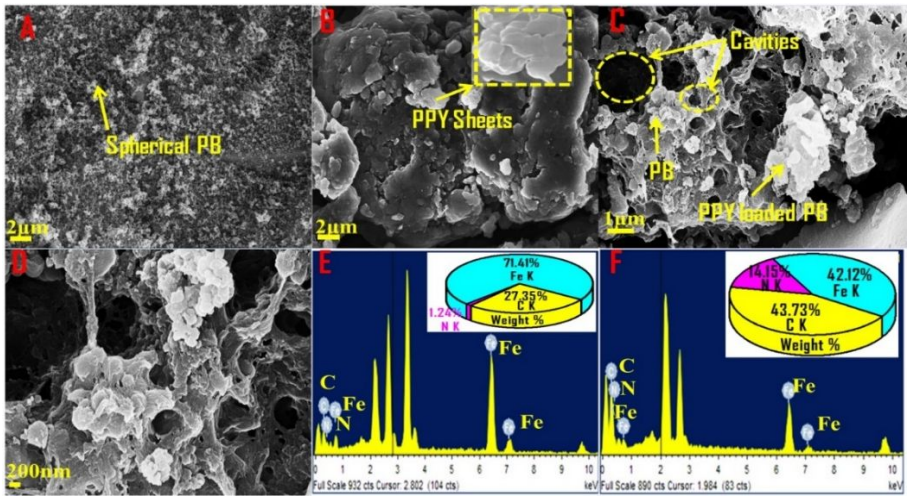

Figure 3. FE-SEM micrographs of (A) PB,(B) PPY, and (C and D) PPY/PB. Corresponding EDX analysis of (E) PB and (F) PPY/PB.

beneficial for mass transfer and pore accessibility during the adsorption process. To determine the composition of synthesized materials, elemental analysis was carried out and the results are depicted in Figure 3 (E and F). The EDX spectra of PB (Figure 3(E)) and PPY/PB nanocomposite (Figure 3(F)) indicate the presence of C, N, and Fe elements with a higher percentage of C and N for the later, confirming the successful incorporation of PB into the PPY matrix (inset of Figure 3(F)). The absence of any additional element in the synthesised samples suggests the high purity of PB dopant and of the PPY/PB nanocomposite. The elemental distribution was further examined through elemental mapping analysis (shown in Figure S3 and S4), which confirmed the uniform distribution of C, N and Fe elements in the PB and nanocomposite. To gain deeper insights into the microstructure of the PPY/PB composite, TEM analysis was utilized. The ImageJ software was employed to estimate the particle sizes from the Gaussian fitting of respective histograms. The dopant exhibited a spherical shaped morphology with an average particle size of 2 nm (inset of Figure 4 (A)). This shape was retained in the nanocomposite. The TEM micrographs of the nanocomposite showed agglomeration of PPY chains in which spherical PB dopant are uniformly dispersed (Figure 4 (B and C)).The average particle size of nanocomposite is around 18 nm (inset of the Figure 4(D) which is large as compared to the size of the pure dopant, confirming their encapsulation in the PPY matrix. At higher magnification (Figure 4 (D and E)), the compact morphology of the nanocomposite was unveiled, as all PB particles seem to be agglomerated in the composite. This result indicates the strong interaction between PB nanoparticles and PPY chains probably via non-covalent forces as well as a good nucleating effect of PPY chains. The electron diffraction pattern (Figure 4 (F)) of the corresponding sample area evidenced the polycrystalline nature of the nanocomposite. The rings with varying diameters, corresponding to different d-spacing values, indicate the presence of distinct crystallographic planes within the material as found in the PXRD pattern of PB.

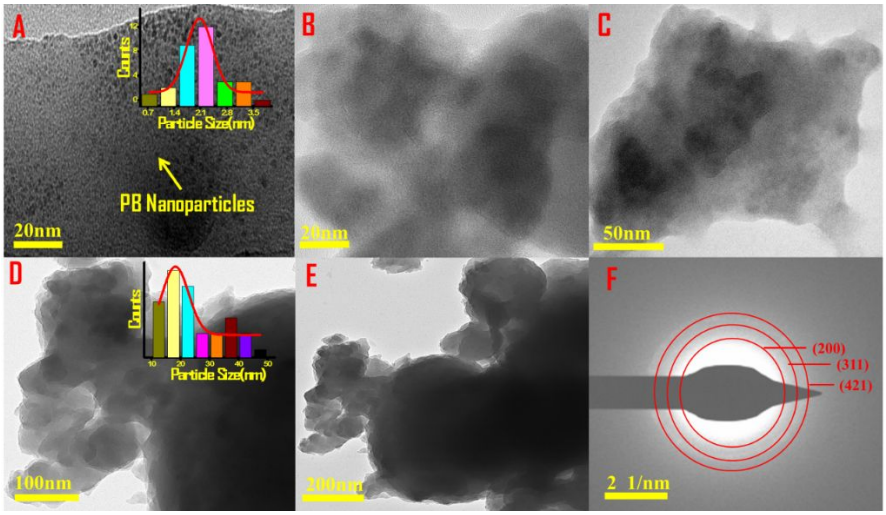

Figure 4. TEM observations of (A) pristine PB and (B-E) the PPY/PB nanocomposite at different magnifications. Insets show the histogram plots for the average particle size distribution fitted by a Gaussian function. (F) Electron diffraction pattern of the PPY/PB nanocomposite.

Electrochemical characterization

Cyclic voltammetry (CV) was employed to analyze the electrochemical behaviour, surface area, and kinetics of PB and the PPY/PB nanocomposite following their deposition on glassy carbon electrodes (GCE).[40,41] The voltammograms of an electrochemical probe 6mM $K_3[Fe(CN)_6]$ with 0.1M KCl as electrolyte were recorded on PB and PPY/PB modified electrodes at various scan rates (Figure 5). The PB-modified electrode shows two pairs of redox peaks, which are typical redox events showing the presence of PB. The first pair of redox waves exhibiting an oxidation peak at 0.37 V and a reduction peak at 0.01 V is attributed to the Prussian white/PB redox. The second pair of peaks with anodic and cathodic peaks positioned at 0.85 V and 0.78 V respectively is assigned to the redox process between PB and Berlin Green.[42] The redox couple towards negative potentials (Prussian white/PB) is due to high spin iron coordinated to nitrogen and the other at more positive potentials (PB/ Berlin Green) is because of low spin iron coordinated to carbon.[43] These electrochemical signatures are also observed in PPY/PB modified GCE with shifting of peaks confirming the incorporation of PB in the nanocomposite. The peak-to-peak separation (ΔEp) value of Prussian white/PB redox of PB/GCE electrode (0.38V) was significantly decreased to 0.11 V for the composite at the same scan rate (100mV/s) indicating that the rate of electron transfer was enhanced at the PPY/PB electrode. In addition, the higher peak current of PPY/PB/GCE compared to PB/GCE could be ascribed to the presence of the PPY matrix enabling a synergistic effect between PB and PPY at the electrode surface for the transport of charge carriers with the increased effective area. To further support these findings, the electroactive surface area of the different electrodes was calculated using the Randles-Sevcik equation:

$$I_{pa} = 2.69 \times 10^5 n^{3/2} A C D^{1/2} v^{1/2}$$

Where I_{pa} is the oxidation peak current (μA), C is the concentration of the redox probe (mol/L), A is the electroactive area (cm^2), D is the diffusion coefficient of the redox probe ($6.7x10^{-6} cm^2/s$), n is the number of electrons transferred and v is the scan rate (V/s).

The cyclic voltammetry studies of PB/GCE and PPY/PB/GCE were carried out in the same electrolyte solution at different scan rates (from 20 mV/s to 100 mV/s). From the slope of the plot of IP vs $v^{1/2}$, the electroactive values obtained are 0.008 cm^2, 0.010 cm^2, and 0.024 cm^2 for bare GCE, PB/GCE, and PPY/PB/GCE respectively. Therefore, the greater electrochemical reactivity obtained with PPY/PB modified electrodes can be attributed to its larger active surface area that enables more adsorption of analytes on its surface. Moreover, the effect of scan rate on the CV plots of PB/GCE and PPY/PB/GCE was investigated to know the kinetics of electrode reactions. As evident from Figure 5 (D and B inset), the peak current varies linearly with the square root of the scan rate, suggesting a diffusion-controlled process at both electrodes.

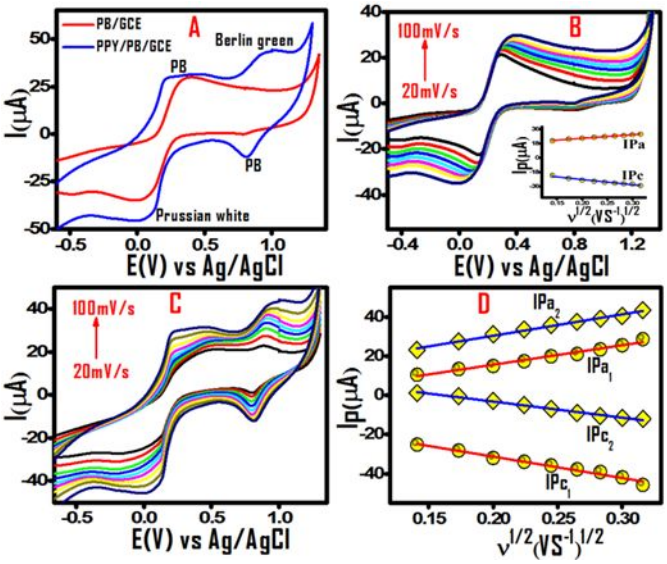

Figure 5. CV responses of modified electrodes in 6 mM $[Fe(CN)_6]_3$ containing 0.1M KCl. (A) comparative CVs of PB/GCE and PPY/PB/GCE at 100 mV/s. (B and C) Voltammograms recorded for PB and PPY/PB modified GCE nanocomposite with changing scan rates (from 20 to 100 mV/s). (D and inset of the figure B) Evolution of the peak intensity (I_p) as a function of $v^{1/2}$ and the resulting linear fits.

Evaluation of the adsorption of PPY/PB towards industrial M.G dye and antituberculosis INH drug

Effect of pH. The solution pH can influence both the surface charge and functional groups on the adsorbent while changing the degree of ionization of contaminants. Therefore, the effect of pH on the adsorption capacity of PPY/PB nanocomposite towards M.G (20 mg/L) and INH (50 mg/L) was studied. As shown in Figure 6(A), the highest PPY/PB adsorption capacity for M.G (15.4 mg/g) was achieved at pH 7 with a removal capacity of 71 %, which is a promising result from the wastewater treatment perspective. The lower adsorption capacity (14.2 mg/g, 65.6 % M.G removal), obtained under acidic conditions, is attributed to positive ionization of the PPY/PB surface by protonation of the nitrogen atom of pyrrole rings.[17] The same process leads to ionization of M.G at pH values below 7,[44] resulting in lowering its adsorption in acidic media. No adsorption tests were performed under alkaline pH for M.G because the dye lost its colour (beyond pH 8.5) indicating a pH-triggered molecular reaction forming new species.[45,46] The observed results of the pH effect on the adsorption of M.G. over PPY/PB nanocomposite were supported by zeta potential studies (Figure 6(c)). The point of zero charge (pH_{pzc}) for the PPY/PB nanocomposite was found at a pH of 3.99, implying that below this pH its surface is positively charged and negatively charged above it. The maximum negative value of the zeta potential is attained at pH 7. Therefore, the attractive interaction of the dye with the composite at pH 7 and repulsive interaction at acidic pH are confirmed. In addition to electrostatic forces, interactions including π-π stacking and hydrogen bonding are also possible between PPY

and M.G. In the case of the sorption of INH antibiotic, adsorption propensities and removal efficiency (%) increased from 8.2 mg/g (16.7 %) to 29.3 mg/g (58.7 %) with the increase in pH from 4 to 7 (Figure 6(B)). Further increase in pH decreased the adsorption capacity to 24.8 mg/g. As INH is amphoteric, it has multiple ionisable groups generating different species as a function of pH. Its acid ionization constants of 1.8, 3.5, and 11.4, arise as a result of the protonation of terminal nitrogen of the hydrazide and heterocyclic nitrogen of the pyridine ring under acidic conditions and loss of a proton from the amide nitrogen atom in basic pH conditions respectively.[47,48] Under acidic conditions (below pH 4) INH mainly exists in its cationic form in aqueous solutions, while the surface of PPY/PB nanocomposite is also positively charged, thus the adsorption capacity decreases due to repulsive interactions. The higher INH adsorption at pH 7 is ascribed to hydrophobic interactions and hydrogen bonding [49] between the nanocomposite and INH. Similarly, the decrease in adsorption uptake above pH 8 is due to the repulsion between the anionic form of INH and the negatively charged surface of the nanocomposite. Regardless of electrostatic repulsion, adsorption still occurs under these pH conditions, indicating that π- π stacking could also make a contribution to contaminant adsorption over PPY/PB. Thus, both pH and zeta potential studies point towards a maximum adsorption of both M.G and INH on PPY/PB nanocomposite under the environmentally viable condition of neutral pH. The possible interaction mechanism between PPY/PB and contaminants is presented in Figure 6(D). Similar mechanism has been described for the adsorption of Methyl Orange and Eosin Yellow dye removal onto conducting polymer-based nanocomposite.[50]

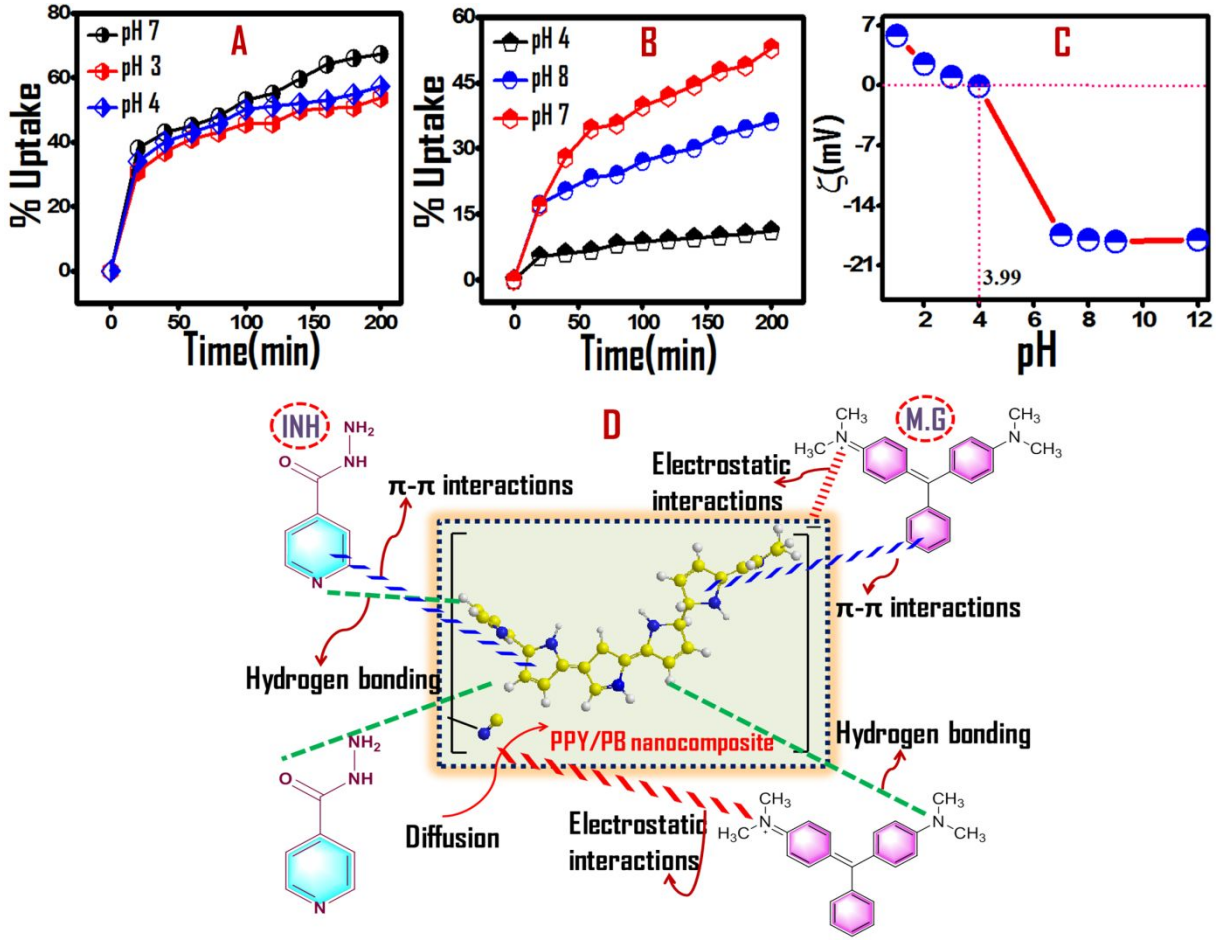

Figure 6. Effect of the pH on the removal efficiency of (A) M.G and (B) INH with initial concentrations of 20 mg/L (M.G) and 50 mg/L (INH). Experiments were carried out using 200 mL of a 1 mg/mL dispersion of PPY/PB at pH = 3-8, T=298 K, for 20 to 200 min. (C) Zeta potential analysis of the PPY/PB nanocomposite. (D) Proposed adsorption mechanism of M.G and INH onto the PPY/PB nanocomposite

Effect of the contact time. The investigation of contact time is a crucial adsorption parameter of an adsorbent. The percentage removal of M.G and INH under different time intervals using PB, PPY, and PPY/PB nanocomposite is presented in Figure 7 (A and B). The adsorption capacity and removal efficiency for the first 60 min increased sharply before levelling off and stabilizing after 180 min, indicating that equilibrium had been established. The faster adsorption for short contact time can be explained by the presence of initial available active sites on the surface of the adsorbent, resulting in bulk interaction with adsorbate molecules. As contact time progresses, the decrease in the rate of adsorption is due to the lowering number of active sites. The effect of contact time on M.G and INH removal was evaluated in the presence of PB, PPY, and PPY/PB nanocomposite.[51] The observed uptake percentage of M.G dye (20 mg/L) and INH (50 mg/L) at the equilibrium stage is 71% and 59% respectively. The performances of the PPY/PB nanocomposite were compared to that of PB and PPY used separately and under similar adsorption conditions. Removal rates of M.G and INH using pure PB were 8% and 7.6% respectively, while PPY removed 15% and 12% of the contaminants (Figure 7(A and B)). The improved adsorptive propensity of PPY/PB is attributed to its increased surface area and porosity, which favour the mass transfer and sorption of M.G and INH on the nanocomposite.

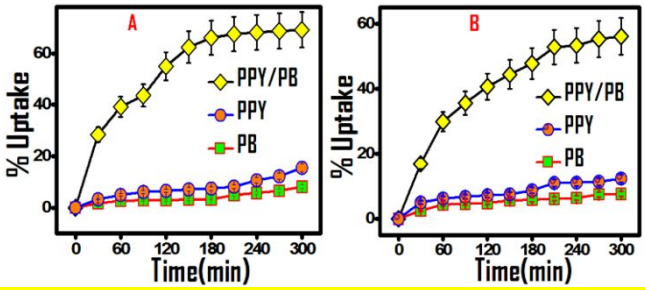

Figure 7. (A) Comparison of the Effect of the contact time on the removal efficiency of (A) M.G (20mg/L) and (B) INH (50mg/L) at pH 7 and 298 K using PB, PPY, and PPY/PB nanocomposite. Experiments were carried out using 200 mL of a 1 mg/mL dispersion of PPY/PB.

Effect of the initial adsorbate concentration. The key parameter in the adsorption process is to determine the appropriate contaminant concentration due to its direct relevance on removal efficiency and the amount of adsorbent required . The influence of initial concentrations of M.G dye and INH drug on the adsorption capacity of PPY/PB nanocomposite was investigated under ambient conditions (pH=7, 298 K) by varying the initial dye and drug concentrations from 5-30 mg/L and 10-60 mg/L respectively (Figure S5 (A, C)). It can be inferred from Figure S5(A) that the adsorption capacity increases from 6.4 to 15.4 mg/g for M.G with a change in concentration from 5-20 mg/L and then shows a decreasing trend with further increase in initial M.G dye concentration. An increase in initial pollutant concentration augments the concentration gradient which amplifies the thermodynamic driving force for the transfer of pollutants from the solution phase to the adsorbent surface.[52-54] However, the removal efficiency of M.G by PPY/PB decreases (95% - 41.8%) with the increase in pollutant concentration from 5-30 mg/L which is attributed to the availability of a sufficient number of active sites at low concentrations resulting in the rapid uptake of pollutants from the bulk. The occupancy to the same active sites becomes difficult with the increasing pollutant concentration due to repulsions between the solute molecules on the adsorbent and bulk phases leading to a decline in overall adsorption efficiency. Similarly for INH uptake, adsorption capacity rises from 9.9-29.3 mg/g under initial concentration change from (10-50 mg/L) and then decreases (Figure S5(C)). Therefore, the optimal concentration for further studies was found to be 20 mg/L for M.G dye and 50 mg/L for INH.

Effect of the adsorbent dosage. The effect of PPY/PB dosage on M.G and INH adsorption is shown in Figure S5 (B and D). The results showed that the adsorption capacity increases from 11.9 to 15.4 mg/g for M.G and 11 to 29.3 mg/g for INH by increasing the adsorbent dose from 150 to 200 mg.The enhancement in removal efficiency and adsorption capacity at a fixed adsorbate concentration with increasing adsorbent doses may be ascribed to the greater adsorbent surface area, thus providing a large number of binding sites to adsorb M.G and INH contaminants.[55] Furthermore, a continuous increase in the adsorbent dose beyond the optimum level lead to a reduction in the adsorption capacity as well as removal efficiency for both adsorbates. This is because at higher doses, overlapping of adsorption sites takes place resulting in a lowering of overall effective surface area.[56] Under these conditions, diffusion of adsorbate molecules to approach adsorbent reactive sites gets prevented resulting in a decreased removal efficiency. Thus 200 mg was observed to be the optimum dosage for selected initial concentrations and chosen contact time for subsequent control experiments.

Adsorption kinetics. Adsorption rate is another crucial factor in predicting the adsorption efficiency of a contaminant over an adsorbent. The standard kinetic models: pseudo-first order (PFO), pseudo-second order (PSO), Elovich and Weber-Morris model (Intraparticle diffusion model (IPD)) were employed for modelling the adsorption kinetics of M.G and INH onto the PPY/PB nanocomposite. The kinetic analysis for the M.G and INH adsorption by PPY/PB was done at six different concentrations in the range of 5-30 mg/L for M.G and 10-60 mg/L for INH. The nonlinear equations (1-4)[57,58] describing the four kinetic models are given below.

$$\text{PFO: } q_t = q_e(1 - e^{-k1t}) \quad (1)$$

$$\text{PSO: } q_t = q_e\left(1 - \frac{1}{k_2\, q_e\, t+1}\right) \quad (2)$$

$$\text{Elovich: } q_t = \frac{1}{\beta} ln\,(\alpha\beta t + 1) \quad (3)$$

$$\text{IPD: } q_t = K_{ipd} t^{0.5} + C \quad (4)$$

Where q_t (mg/g) is the amount of adsorbate adsorbed at time t; q_e (mg/g) is the amount of adsorbate adsorbed at equilibrium; k1 is the rate constant for PFO (min^{-1}); k2 is the rate constant for PSO (g/(mg/min); β (g/mg) and α (mg/g/min) are the desorption constant and initial adsorption rate; K_{ipd} is the intraparticle diffusion rate constant ($mg/g/min^{-0.5}$) and C is the intercept related to thickness of the boundary layer (mg/g).

All observed kinetic parameters are presented in Table 1 and the corresponding curves are given in Figure 8. As reflected in Table 1, the correlation coefficients of pseudo-second order and Elovich model are higher than that of pseudo-first order model at all concentrations of M.G and INH. The chi-square (χ^2) values of both models are smaller in comparison to the Pseudo-first order. Furthermore, the q_e (mg/g) calculated values of pseudo-second order model are closer to the experimental values for M.G and INH. Thus both pseudo-second order and Elovich model make the best fit to experimental data, implying that adsorption of M.G and INH onto PPY/PB nanocomposite follows the chemisorption process in which chemical bonds between the adsorbent active sites and adsorbate molecules are formed through share or exchange of valence electrons. [59] This also implies that M.G and INH initially get first adsorbed on the nanocomposite's external surface but subsequently diffuse and adsorb into the interior sites as the active sites of the adsorbent get fully occupied. Although the calculated and experimental values of q_e were much closer for the Pseudo-first order model but due to its lower R^2 and higher χ^2 values, it cannot be the acceptable adsorption kinetic mechanism. To predict the diffusion mechanism and rate-limiting step of M.G and INH adsorption onto the PPY/PB surface, an intra-particle diffusion model was applied. The R^2 values for INH are higher than for M.G (Table 1). As depicted in Figure 8 (D and H), the plot of IPD did not pass through the origin suggesting that intraparticle diffusion mechanism alone cannot explain the M.G and INH uptake by PPY/PB adsorbent.[60] This observation further validates that the adsorption of M.G and INH on the adsorbent occurred through a multi-step process. Figure 8 (D and H), shows two stages, the initial stage represents the faster uptake of M.G and INH from the aqueous phase to the adsorbent's external surface (film/surface diffusion model). This migration is directly proportional to the surface area of the adsorbent because a higher surface area corresponds to a faster diffusion rate. The diffusion process then slows down at the second stage, implying that less active sites are available for effective adsorption (intraparticle diffusion mechanism).[61] The slope of the second stage gives the K_{IPD} parameter. Besides the larger intercept observed in the second segment (greater than 0), which gives the thickness of the boundary layer, indicating that surface adsorption is also involved in the rate-limiting step. Thus, the adsorption of M.G and INH over PPY/PB involves film dispersion and intraparticle diffusion as potential mechanistic processes. As the diffusion rate constant of INH is greater than that of M.G (Table 1) for the same concentration it diffuses easily into the pores of PPY/PB nanocomposite than M.G leading to its higher adsorption rates. These results are in good agreement with other experimental findings.

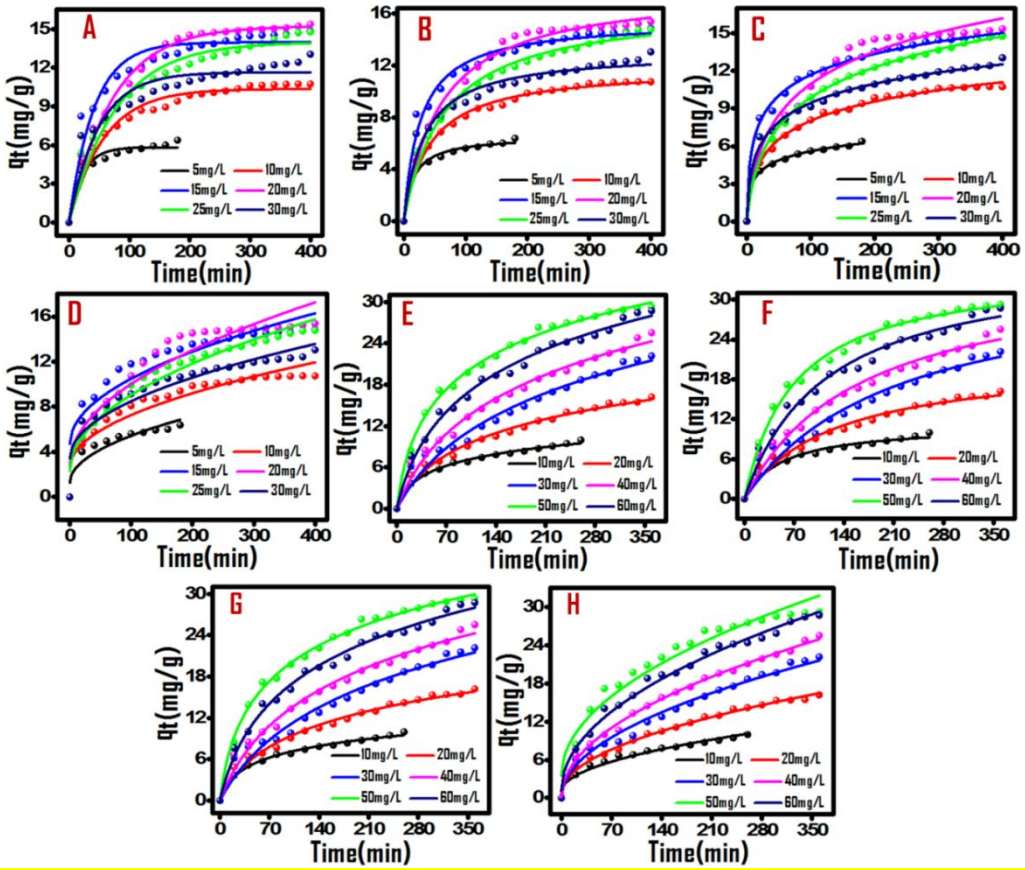

Figure 8. Non-linear fitted curves of different kinetic models; PFO (A, E), PSO (B, F), Elovich (C, G), and IPD kinetic models (D, H) for M.G and INH adsorption respectively onto the PPY/PB nanocomposite at pH 7 and 298 K. Experiments were carried out using 200 mL of a 1 mg/mL dispersion of PPY/PB with contact times of 5 to 400 min (M.G) and 5 to 360 min (INH). Initial adsorbate concentrations varied from 5 to 30 mg/L (M.G) and 10 to 60 mg/L (INH).

Table 1. Adsorption kinetic parameters after non-linear fitting for the adsorption of M.G and INH onto PPY/PB adsorbent at pH 7 and 298 K. Experiments were carried out using 200 mL of a 1 mg/mL dispersion of PPY/PB with contact times of 5 to 400 min (M.G) and 5 to 360 min (INH). Initial adsorbate concentrations were varied from 5 to 30 mg/L (M.G) and 10 to 60 mg/L (INH).

Adsorbate	Pseudo-1st order					Pseudo-2nd order			
	C_0	$q_{e,exp}$	$q_{e,cal}$	k1	R^2	k2	$q_{e,cal}$	R^2	χ^2
M.G	5	6.38	5.83	0.04	0.96	0.01	6.54	0.99	0.04
	10	10.74	10.4	0.02	0.96	0.002	11.8	0.99	0.07
	15	14.84	13.97	0.024	0.93	0.0024	15.45	0.98	0.23
	20	15.37	15.24	0.014	0.98	0.0009	18	0.98	0.25
	25	14.77	13.98	0.013	0.96	0.00093	16.65	0.99	0.18
	30	13.04	11.65	0.009	0.89	0.0023	13.06	0.96	0.33
INH	10	9.96	9.15	0.016	0.95	0.002	11.14	0.98	0.14
	20	16.2	16.22	0.008	0.96	0.00038	21.04	0.97	0.47
	30	22.16	24.5	0.005	0.95	0.00014	34	0.96	1.34
	40	25.53	25.9	0.007	0.97	0.00017	34.9	0.98	1.07
	50	29.266	28.6	0.013	0.97	0.0004	34.72	0.99	0.48
	60	28.73	28.14	0.009	0.97	0.00024	36.2	0.98	1.12

Adsorbate	Elovich model				Intraparticle diffusion (IPD) Model			
	C_0	α	β	R^2	χ^2	K_{IPD}	C	R^2	χ^2
M.G	5	2.13	0.95	0.99	0.008	0.42	1.25	0.86	0.48
	10	0.77	0.44	0.99	0.03	0.47	2.59	0.89	0.75
	15	2.98	0.412	0.99	0.05	0.58	4.69	0.83	2.01
	20	0.6	0.25	0.97	0.45	0.72	2.79	0.89	1.78
	25	0.5	0.27	0.99	0.03	0.67	2.33	0.95	0.63
	30	1.5	0.45	0.99	0.06	0.51	3.42	0.88	2.8
INH	10	0.36	0.38	0.99	0.05	0.56	0.99	0.97	0.19
	20	0.24	1.17	0.98	0.26	0.83	0.64	0.99	0.12
	30	0.197	0.095	0.97	1.05	1.14	0.09	0.98	0.52
M.G	40	0.27	0.097	0.98	0.67	1.31	0.06	0.99	0.19
	50	0.85	0.122	0.99	0.27	1.49	3.54	0.96	2.63
	60	0.45	0.102	0.99	0.56	1.47	1.23	0.99	0.58

Equilibrium studies

The correlation between the amount of M.G and INH adsorbed on the PPY/PB nanocomposite and its maximum adsorption capacity can be best described by adsorption isotherms. Non-linear isotherm models, including Langmuir, Freundlich, Temkin, and Redlich-Peterson models were employed to fit the experimental data.

Langmuir model is based on the assumption of a monolayer adsorption onto the homogenous surface of adsorbent without any lateral interactions between the adsorbate molecules.[62] The separation factor (R_L) is an important parameter in Langmuir isotherm that determines the feasibility of the adsorption process. The adsorption process will be favourable if $0<R_L<1$, unfavourable ($R_L>1$), linear ($R_L=1$), or irreversible ($R_L=0$).[58,62] The Freundlich isotherm elucidates the adsorption process as a multilayer formation on a heterogeneous surface of adsorbent. The Temkin isotherm considers the interaction between adsorbent and adsorbate molecules with a linear decrease of adsorption heat with the surface coverage.[63] The value of the Temkin constant enables determining whether physical or chemical adsorption occurs on the adsorbent surface. If $b_T>40$ kJ/mol, chemisorption occurs, and if $b_T<40$ kJ/mol, physisorption proceeds.[63] The Redlich-Peterson model is a combination of Langmuir and Freundlich isotherm models applicable for homogenous and heterogeneous adsorption processes. When the g parameter is equal to 1 and 0, the R-P model becomes the Langmuir equation and Freundlich equation respectively.[64] The nonlinear equations of isotherm models are expressed as:

Langmuir: $$q_e = \frac{q_m k_L C_e}{1+K_L C_e} \quad (5)$$

$$R_L = \frac{1}{1+K_L C_0} \quad (6)$$

Freundlich: $$q_e = K_F C_e^n \quad (7)$$

Temkin: $$q_e = B ln(A_T C_e);$$

$$B = \frac{RT}{b} \quad (8)$$

Redlich-Peterson: $$q_e = \frac{K_{RP} C_e}{1+\alpha_{RP} C_e^g} \quad (9)$$

where C_e (mg/L) is the equilibrium concentration of M.G and INH, q_m (mg/g) is the maximum adsorption capacity, K_L is the Langmuir binding constant (L/mg), R_L is the separation factor related to adsorption feasibility. K_F is the Freundlich constant which gives strength of adsorption ((mg/g (L/mg)^n) and n is the adsorption intensity parameter; A_T is the equilibrium binding constant (L/mg), b_T is the Temkin constant (kJ/mol) related to the heat of adsorption, T is the temperature (K) and R (J/mol/K) is the universal gas constant; α_{RP} and K_{RP} are the R-P constants corresponding to affinity of the binding sites and adsorption capacity respectively and g is an exponent which gives adsorption intensity ($0< g < 1$).

The observed isotherm parameters are summarised in the Table 2 and the respective plots are given in the Figure S6. Out of four models, Langmuir and R-P models displayed the highest R^2 (0.99) and lowest χ^2 values for M.G and INH. Also, the maximum adsorption capacities calculated from the Langmuir model (15.8 mg/g for M.G and 34.3 mg/g for INH) were in close agreement with experimental data (15.4 mg/g for M.G, 29.3 mg/g for INH). This means that the Langmuir model is the most suitable model for explaining the adsorption mechanism of M.G and INH onto the PPY/PB. Also, the R_L values for both adsorbates lie in between 0 and 1 reflecting a favourable adsorption process. From the Temkin isotherm, the lower b_T values for both M.G and INH correspond to physisorption. It was noticed from Table 2, that the g parameter value in the R-P model is equal to 1, meaning that the Langmuir model fits more easily into the adsorption data of both M.G and INH using PPY/PB adsorbent than the Freundlich model.

Table 2. Adsorption isotherm parameters after non-linear fitting for the adsorption of M.G and INH onto PPY/PB adsorbent at pH 7 and 298 K. Experiments were carried out using 200 mL of a 1 mg/mL dispersion of PPY/PB with contact times of 400 min (M.G) and 360 min (INH), and initial adsorbate concentrations Ci=5-40 mg/L (M.G) and 10-60 mg/L (INH).

	Langmuir Model						Freundlich Model			
	$q_{e,exp}$	$q_{m,cal}$	K_L	R_L	R^2	χ^2	K_F	n	R^2	χ^2
MG	15.4	15.75	2.4	0.076	0.97	0.4	10.8	0.19	0.61	4.6
INH	29.3	34	0.22	0.31	0.98	1	9.95	0.34	0.92	4.5

	Temkin Model				Redlich-Peterson Model				
	A_T	b_T	R^2	χ^2	K_{R-P}	α_{R-P}	g	R^2	χ^2
MG	484.2	1.45	0.70	3.52	29.67	1.62	1.05	0.99	0.103
INH	2.29	0.34	0.97	1.75	7.05	0.182	1.03	0.98	1.4

Thermodynamic analysis

The effect of the temperature on the adsorption of M.G and INH onto PPY/PB nanocomposite was monitored at three temperatures under optimum conditions. The thermodynamic studies determine the adsorption feasibility and physicochemical parameters such as Gibbs free energy, entropy change, and enthalpy change. These equations are shown below

$$\Delta G^\circ = -RT\ln(K_d) \quad (10)$$

$$\ln(K_d) = -\Delta H^\circ/RT + \Delta S^\circ/R \text{ (Van't Hoff equation)} \quad (11)$$

The observed thermodynamic parameters are summarized in Table 3 and are calculated from the slope and intercept of the plot of log(K_d) with 1/T of Figure S7 (B and D). The adsorption of M.G and INH decreases with the rise in temperature from 298 to 318 K (Figure S7(A and C)) which indicates that product formation is reduced as the equilibrium of the reaction shifts towards the backward direction. Thus the higher temperature is not favourable for M.G and INH adsorption and their interactions with the PPY/PB are exothermic in nature (ΔH^o is negative). The similar results of the temperature dependence were obtained from the previous reports for the removal of M.G and INH.[47,65,66] The negative value of ΔS^o for both adsorbates signifies the decreased disorder and degree of freedom at the adsorbate-adsorbent interface. The negative ΔG^o at

all temperatures of INH implies the adsorption process is spontaneous and favourable and it increases with the increase in temperature. However, the positive value of ΔG^o in the case of M.G at 318K indicates its less spontaneous adsorption than INH. Moreover, the values of ΔG^o for M.G and INH come in the sphere/range of $-20<\Delta G^o<0$ kJmol^{-1}, which signifies the spontaneous physical adsorption process at the solid-solution interface.[58,67] These results corroborate with the Temkin isotherm model.

Table 3. Thermodynamic parameters for the adsorption of M.G and INH onto PPY/PB adsorbent at pH 7 with T=298-318 K. Experiments were carried out using 200 mL of a 1 mg/mL dispersion of PPY/PB with contact times of 400 min (M.G) and 360 min (INH), and initial adsorbate concentrations of 20 mg/L (M.G) and 50 mg/L (INH).

	Temp (K)	ΔG^O (kJ/mol)	ΔH^O (kJ/mol)	ΔS^O (J/mol K)
MG	298	-1.07	-21.93	-0.07
	308	-0.37	-21.93	-0.07
	318	0.33	-21.93	-0.07
INH	298	-0.39	-5.4	-0.017
	308	-0.226	-5.4	-0.017
	318	-0.0576	-5.4	-0.017

Proposed adsorption mechanism of M.G and INH onto the PPY/PB nanocomposite

To gain an insight into the adsorption mechanism, FTIR and FE-SEM-EDX analysis after adsorption was performed (Figure 9 and figure 10). There occurs appreciable changes in the FTIR spectra after the adsorption of M.G and INH onto PPY/PB nanocomposite (Figure 9). The peak at 3454 cm^{-1} on the spectrum of the nanocomposite (N-H stretching vibration of pyrrole) slightly shifts to a lower wave number (3431 cm^{-1}, 3430 cm^{-1}) with reduced intensity after adsorption, suggesting that N-H groups of PPY are involved in hydrogen bonding with the adsorbed M.G and INH. The other bands at 1638 cm^{-1} and 1383 cm^{-1} in the nanocomposite spectrum shifts to 1628 cm^{-1}, 1630 cm^{-1} and 1392 cm^{-1}, 1380 cm^{-1} which may be due to π-π interactions between PPY and adsorbate (MG, INH) molecules. The bands at 2080 cm^{-1} and 502 cm^{-1} characteristic of -C-N- and Fe-CN stretching frequencies of PB moiety also get decreased and shifted respectively as compared to fresh nanocomposite after adsorption indicating electrostatic interactions with the cationic dye. The structural stability can also be analysed from FTIR spectra as there occurs no noticeable changes in the structural regions of vibration of nanocomposite after the adsorption. To sum up, the adsorption of M.G and INH onto PPY/PB nanocomposite can be due to variety of interactions such as π-π interactions, electrostatic interactions, and hydrogen bonding.[68]

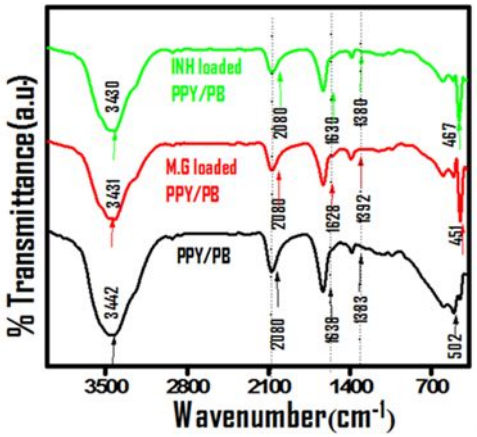

Figure 9. (A) FTIR analysis of the PPY/PB nanocomposite before and after adsorption of M.G and INH.

The diffusion of INH into the interior sites of adsorbent is also possible due to its smaller hydrodynamic diameter compared to M.G. As the molecular structures of both pollutants are different, INH shows additional interactions (hydrogen bonding) than M.G which accounts for its higher adsorption propensity. The proposed mechanism supports the experimental results where the PPY/PB nanocomposite displayed higher adsorption capacity towards INH than M.G. Similarly, from the intraparticle diffusion model, the observed K_{IPD} value is higher for INH leading to its higher removal than M.G. Analysis by FE-SEM-EDX were carried out to observe the morphology and composition of the PPY/PB nanocomposite after the adsorption of M.G dye and INH drug (Figure 10). Post-adsorption observations (Figure 10(A and D)) suggest a rise in particle/granular size of the nanocomposite which is likely attributed to the adherence of contaminants onto the adsorbent surface. Also, the surface of PPY/PB appears more uniform due to the clogging of pores/cavities by the contaminants, thereby validating the adsorption of M.G and INH onto PPY/PB. Nevertheless, the morphology of PPY/PB remained largely unchanged following the adsorption, highlighting its structural stability. After contaminant loading, there was a significant increase in the percentage weight of carbon and nitrogen detected by EDX analisis, corroborating the successful adsorption of contaminants onto PPY/PB (insets of Figure 10 (B and E)).

Adsorption studies of M.G and INH in samples from natural environments. To demonstrate the usefulness of PPY/PB as an adsorbent in real-time application, its adsorption efficiency for M.G and INH removal was further investigated in different water samples including lake water and tap water. It is observed from Figure S8(A) that a minimal decrease in M.G and INH adsorption occurs under optimized conditions when environmental water samples were used, suggesting that PPY/PB may be a potential candidate for wastewater treatment applications.

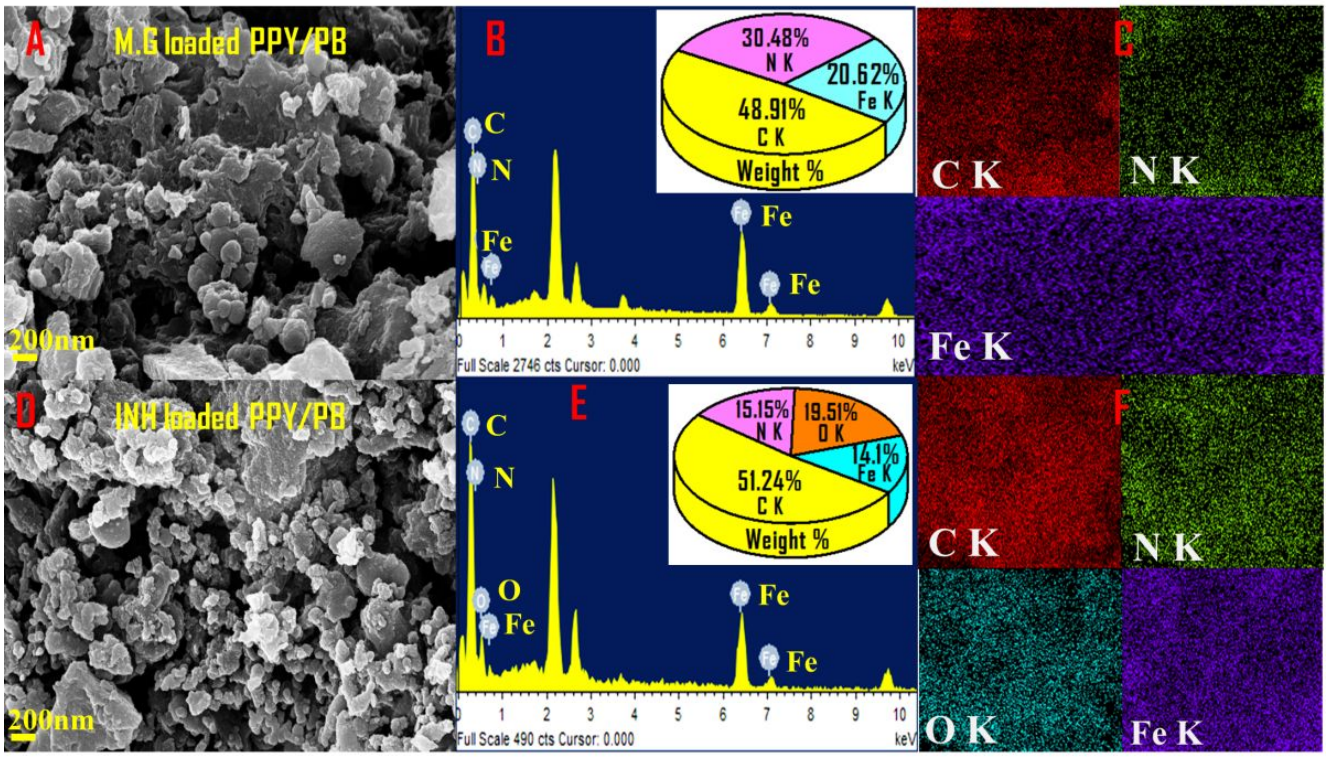

Figure 10. SEM micrographs (A and D), EDX spectra (B and E), and elemental mapping patterns of C, N, O, and Fe (C and F) of the PPY/PB nanocomposite after adsorption of M.G and INH respectively.

Reusability, regeneration and robustness of the PPY/PB nanocomposite as an adsorbent.

For sustainable applications, the adsorbent needs to be regenerated after the adsorption process. The PPY/PB loaded with adsorbate species was treated with 0.1M HNO_3 as the eluting agent. After four cycles of regeneration, the adsorption capacity of PPY/PB nanocomposite for M.G and INH removal slightly decreases to 14 mg/g and 28 mg/g respectively (Figure S8(B)). The efficiency decay during cyclic adsorption is attributed to the inevitable matter and energy losses.[68] These results demonstrate that the PPY/PB nanocomposite displays good regeneration and reusability ability making it suitable for real-time water treatment.

Furthermore, the stability of the PPY/PB nanocomposite under harsh conditions (pH= 3 and 9) was evaluated through FTIR and DR-UV experiments (figure S9 (A)). The FTIR spectra of the nanocomposite remained constant regardless of pH. The stability of the nanocomposite was further confirmed by calculating band gap values from DR-UV analysis and the obtained values were almost the same under these conditions, suggesting similar electronic and optical properties of the PPY/PB nanocomposite(Figure S9 (B)). In addition, interference studies were carried out (Figure S10) to study how the contaminant uptake percentage would change when M.G, INH, and 4-NP are simultaneously put into contact with by PPY/PB. The data revealed that under the optimized experimental conditions, there was no significant change in the removal efficiencies of adsorbates by PPY/PB nanocomposite in a ternary mixture.

Adsorption performance of PPY/PB with other adsorbents for the removal of M.G and INH.

Based on the calculated adsorption capacity and solution pH, the comparison of PPY/PB nanocomposite towards the removal of M.G and INH with other adsorbents in literature[44,48,49,69-77] have been investigated (Table 4). It is clear from the table that the prepared PPY/PB showed the highest adsorption capacity for both M.G and INH at neutral conditions (pH 7, 298K). Although the adsorption capacity of PPY/PB for M.G removal is lower than some of the already known composites, but due to its low cost and simple synthetic procedure, it becomes applicable for treating wastewater.

Synergistic effect of adsorption on catalytic reduction of 4-nitrophenol (4-NP) to 4-aminophenol (4-AP)

Although adsorption is a versatile method of water treatment, it suffers the limitation that contaminants are only trapped on the adsorbent surface without actual degradation or conversion to any of their less toxic form. At the same time, adsorption is crucial for effective photocatalysis or surface catalysis. Thus, the synergy between adsorption and degradation is very important for efficient and effective decontamination of persistent contaminants for sustainable water treatment. An ideal or perpetual water treatment method would be a process that very effectively adsorbs contaminant under environmentally viable conditions and post-surface concentration (on adsorbent) cumulated with a faster visible light mineralization.

Table 4: Comparison of adsorption capacities of the PPY/PB nanocomposite with other adsorbents for M.G and INH removal

Adsorbent	q_m (mg/g)	pH	$t_{Contact}$ (min)	Ref.	Adsorbent	q_m (mg/g)	pH	$t_{Contact}$ (min)	Ref.
		M.G					INH		
Mn-Fe LDH /PES composite	13.5	7	60	69	Graphene Oxide	13.9	2	60	70
Carbon nanotube/ Polyaniline	15.4	7	60 120	71	Bentonite	21.1	<4	20	48
Catha edulis stem	5.6	10	60	44	Organobentonite	33.9	<4		48
Unsaturated polyester Ce(IV) phosphate	1	8	30-35	72	Perlite	0.1		30	49
Rice Husks	6.5	7	100	73	Kaolinite	0.8			49
Mesoporous Chitosan-Zinc oxide	11	8	180	74	Vermiculite	0.1			49
MWCNT-COOH	11.7	9	10	75	PPY/PB	34	7	180	This work
Activated carbon	19.9	6	3	76					
Citric acid-treated pea shells	17.2	7	35	77					
PPY/PB	15.8	7	180	This work					

This dual action would enable self-cleaning the adsorbent for as many further decontamination cycles as possible. Towards this endeavour, we evaluated the reduction of toxic 4-nitrophenol (4-NP) to 4-aminophenol (4-AP) using ($NaBH_4$) as a reducing agent. When 4-NP was put into contact with the PPY/PB nanocomposite in the presence of visible light (Figure S11 (A)) only adsorption of 4-NP occurred without any reduction to 4-AP, precluding the photo-redox-based reduction possibility. A similar result was obtained from PPY/PB mixtures under dark conditions without the addition of $NaBH_4$ (Figure S11 (B)). In addition, in the presence of only $NaBH_4$ as a reducing agent under dark or visible light irradiation, no reduction of 4-NP to 4-AP was observed over an extended time, suggesting the kinetic constrains to this reduction. In contrast, when the reaction mixture contained both $NaBH_4$ and the PPY/PB nanocomposite, the reduction of 4-NP to the 4-AP was achieved in less than 10 minutes under dark conditions. The rates of nitrophenol reduction became faster with increasing weight percent of PPY/PB, confirming the surface catalyst-based synergistic effect on the nitrophenol reduction (Figure 11(B-D)). The surface catalytic effect of synthesized PPY/PB composite for reduction of 4-NP to 4-AP in the presence of $NaBH_4$ as a reducing agent was monitored spectrophotometrically. The UV–-visible spectra of pure 4-NP shows a sharp peak at 317 nm which shifts to 400 nm (Figure 11 (A)) in the presence of $NaBH_4$ owing to the formation of nitrophenolate ion.[78] In the presence of $NaBH_4$ alone, no appreciable decrease in absorption peak of 4-NP was obtained after 90 min suggesting that $NaBH_4$ alone cannot reduce 4-NP (Figure 11(A)). This can be attributed to the high potential energy barrier between donor $NaBH_4$ and acceptor 4-NP.[79] However, in the concomitant presence of both $NaBH_4$ and the PPY/PB nanocomposite, the intensity of the absorption peak at 400 nm rapidly declines and the appearance of a new intense peak at 315 nm confirms the formation of 4-AP [80,81] which is also depicted from the colour change (Figure S12). The complete reduction to 4-AP occurs within 4 min in the presence of 30 mg of catalyst (Figure 11 (D)).

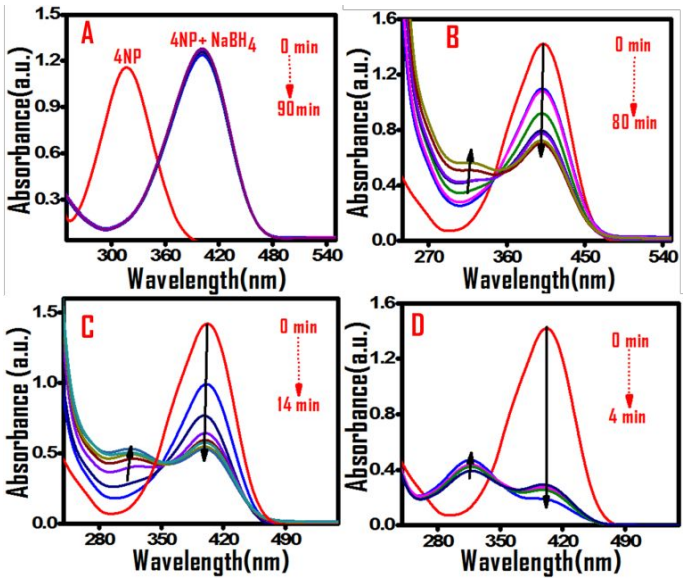

Figure 11. Time-dependent UV-Vis Plots of 4-NP(0.1 mM) in the presence of $NaBH_4$ (2mM) as a reducing agent at different PPY/PB catalyst amounts (A: without catalyst, B:15 mg, C:20 mg, and D:30 mg

Table 5. Kinetic parameters obtained for reduction of 4-NP to 4-AP under different experimental conditions.

PPY/PB dose (mg)	k (min^{-1})	% Conversion (after 5min)	R^2	$NaBH_4$ (mM)	k (min^{-1})	R^2	4-NP (mM)	k (min^{-1})	R^2
4-NP=0.1mM $NaBH_4$ =2mM				4-NP=0.1mM PPY/PB=0.02g			$NaBH_4$=1mM PPY/PB=0.02g		
Without catalyst	0.001	3% (90min)	0.99	1	0.178	0.98	0.05	0.175	0.97
15	0.024	11.8%	0.99	2	0.08	0.98	0.1	0.2	0.96
20	0.077	50.83%	0.99	3	0.023	0.98	1	0.233	0.98
30	0.280	90%	0.98						

The rate of reaction does not depend on $NaBH_4$ concentration taken in excess; thus pseudo-first order kinetics can be used to evaluate rate constants for the catalytic hydrogenation of 4-NP. The apparent rate constants were calculated by using the following equation.[78]

$$ln\frac{C_t}{C_i} = -kt \quad (12)$$

where k is the apparent rate constant, C_t and C_i are the 4-NP concentration at time t and time 0 respectively.

The effect of the catalyst dose on the 4-NP reduction in the presence of $NaBH_4$ was also studied (Figure 11(B-D)) and their kinetic plots and conversion rate to 4-AP are given in Figure S13. The values of the rate constant increase with the increase in catalyst amount from 15 mg to 30 mg and are presented in the Table 5. This is due to the presence of more available active sites on the catalyst surface as the dosage is increased. For the catalytic recudtion of 4-NP to 4-AP, the influence of 4-NP and $NaBH_4$ concentrations was investigated by keeping the concentration of PPY/PB catalyst constant to 20 mg (Figure S14 and S15). The values of apparent rate constants increase as the concentration of 4-NP increases from 0.05 mM to 1 mM and decrease on increasing the $NaBH_4$ concentration from 1 mM to 3 mM (Table 5). Thus 1:1 ratio of 4-NP and $NaBH_4$ is suitable for catalytic reduction under synergistic adsorption-activated catalysis.

Mechanism for the catalytic reduction of 4-NP

The high surface area of the PPY/PB nanocomposite allows good surface properties for the catalytic reduction of 4-NP to 4-AP. The Langmuir-Hinshelwood model can be applied to describe the reaction mechanism of catalytic reduction of 4-NP.[79] Initially, $NaBH_4$ gets adsorbed on the surface of PPY/PB as borohydride ions. The adsorbed BH_4^- ions generate active hydrogen on the catalyst surface to reduce 4-NP in a multistep process *via* the formation of a stable intermediate (Scheme 2). Ater reduction, the adsorbed 4-AP gets desorbed from active sites on the catalyst surface enabling the next catalytic cycle.

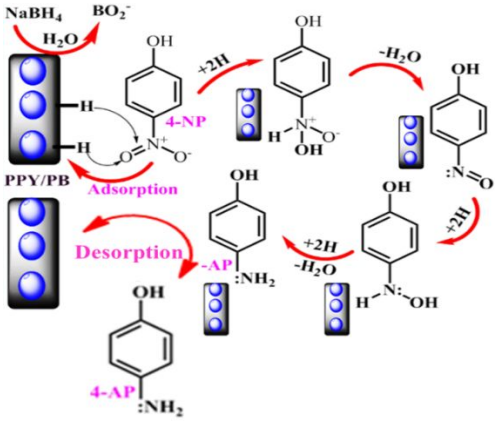

Scheme 2 Plausible mechanism of the reduction of 4-NP to 4-AP by $NaBH_4$ over the PPY/PB nanocomposite acting as both an adsorbent and a catalyst.

Experimental

Materials and methods

The reagents potassium ferricyanide, chloroform, and anhydrous ferric chloride used in the synthesis of PPY/PB nanocomposite were of analytical grade (Himedia, India) and were used without further treatment except pyrrole (stored at -5°C).

The functional groups and chemical bonds of the synthesized materials were characterized using an FTIR spectrophotometer (Alpha Bruker) in a mid-frequency region (400-4000 cm^{-1}). Thermogravimetric analysis for determining the thermal behaviour and decomposition was carried out on a SEIKOTG/DTA 6200 instrument between 25°C to 800°C at a heating rate of 10°C under a nitrogen environment. The structural properties of samples were done on powder X-ray diffraction (PXRD, PW3050 diffractometer). The crystallite size was calculated from the most intense diffraction peak with 2θ=17.31°, FWHM=0.275° for PB nanoparticles and 2θ=17.36°, FWHM=0.76° for the nanocomposite by using Scherrer's equation [82] as mentioned in equation 13

$$D = \frac{K\lambda}{\beta Cos\theta} \quad (13)$$

Where K= 0.9 is the shape factor, λ is the wavelength of the X-ray, β is the full width at half maximum (FWHM) and θ is the diffraction angle.

Transmission electron microscopy (TEM) measurements were performed on a TEM Hitachi (H-7500) for analysing the particle morphology and size. SEM-EDX images were captured using a ZEISS Gemini SEM 500 instrument operating at 15.00kV. Nitrogen adsorption-desorption measurements were obtained at 77K using a Quantachrome Autosorb IQ Station BET instrument. Prior to measurements, samples were degassed under vacuum at 200°C for 3h. The surface area was calculated using the Brunauer-Emmett-Teller (BET) method and the corresponding pore size distribution was obtained by the non-local density functional theory (NLDFT) equilibrium model. For determining the surface charge of the PPY/PB nanocomposite, an Anton Par particle size analyzer was used (Litesizer 500). The cyclic voltammetry experiments were carried out on a Bio-Logic SAS potentiostat (Model SP 150) using a conventional three-electrode cell containing 6 mM $K_3[Fe(CN)_6]$ and 0.1M KCl electrolyte solution. The glassy carbon electrode (GCE, 3 mm in diameter), Ag/AgCl, and platinum wire were used as the working electrode, reference electrode, and counter electrode respectively. The adsorption and catalytic reduction studies were performed using a UV-visible spectrophotometer (Double Beam Microprocessor Mode: LI-2802).

Synthetic procedures

Synthesis of PB and the PPY/PB nanocomposite. The PPY/PB nanocomposite was synthesised by oxidative polymerization using $FeCl_3$ as the oxidant in a non-aqueous medium as per our previous work.[22,26,83] The synthetic protocol involves the dropwise addition of anhydrous $FeCl_3$ (0.05 M) in $CHCl_3$ solvent (170 mL) to a stirred solution of pyrrole monomer (0.02 M) containing 1 g of synthesized Prussian Blue (PB) which was ground for about 20 min using a mortar and pestle. The reaction mixture was vigorously stirred for 24 hours so that effective polymerization takes place. Subsequently, the obtained blue precipitate was collected by filtration, washed several times with water and then dried in the oven. For comparison, pure PB was synthesised using an equimolar mixture of anhydrous $FeCl_3$ and $K_3[Fe(CN)_6]$ (0.05 M) under similar conditions in the absence of pyrrole. The overall synthetic procedure of PPY/PB composite is presented in scheme 3.

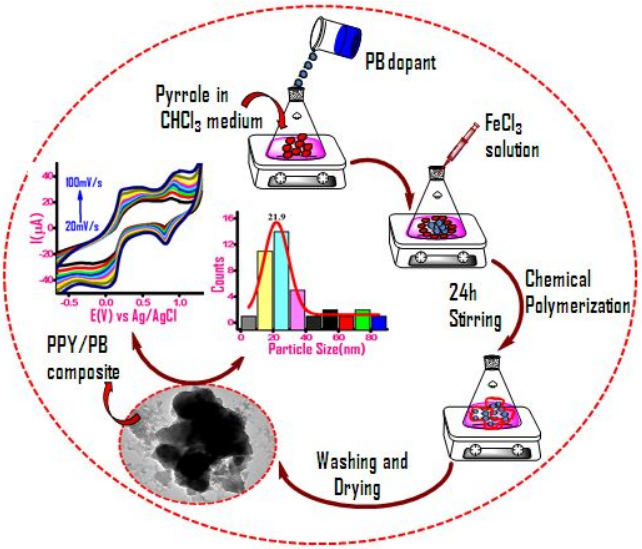

Scheme 3. Schematic procedure for the preparation and characterization of the PPY/PB nanocomposite

Preparation of modified electrodes

Prior to the fabrication of PB and PPY/PB electrodes, the surface of GCE was polished with alumina powder (0.05 µm) followed by washing with triple distilled water and ethanol, and then dried in open air. PB or PPY/PB samples (3 mg) were dispersed in water with 10 µL of nafion as a binder. The mixtures were sonicated for about 40 min to form a homogenous suspension. Then, 4 µL of each suspension was drop casted onto polished GCE and allowed to dry for 1 hour in open air.

Adsorption experiments. The adsorption experiments were performed under dark conditions. The volume of the adsorbate solutions (200 mL) and stirring speed (1200 rpm) were uniform for all experimental procedures. The effect of adsorption parameters like adsorbent dose (150-250 mg), adsorption contact time of 6 hours, initial adsorbate concentration (5-30 mg/L M.G,10-60 mg/L INH), three solution pH (3, 7, and 8) and a temperature range of 25—45°C on the relative adsorption propensity of M.G, INH, and 4-NP was investigated. After regular time intervals of 5.0 min, 3mL aliquots were withdrawn and centrifuged for 5.0 min to remove adsorbent particles. The residual concentrations of pollutants were analysed through UV-visible spectrophotometer[50,84]at λ_{max} of 617 nm, 264 nm, and 317 nm corresponding to M.G dye, INH antibiotic, and NP respectively.[85-87]The concentrations were calculated from the prepared calibration curve using Beer-Lambert law using standard solutions of each adsorbate. The following equations were used to calculate adsorption capacity and % removal.

$$q = \frac{C_0 - C_t}{m}.\mathrm{V} \quad (14)$$

$$\%\mathrm{Removal} = \frac{C_0 - C_t}{C_0}.100 \quad (15)$$

Where m is the mass of PPY/PB nanocomposite (g), C_0 is the initial and C_t is the final concentration of M.G and INH (mg/L), and V represents the volume of adsorbate solution in mL.

Catalytic reduction of 4-NP. The procedure for the catalytic reduction involves the addition of excess $NaBH_4$ (2mM) to a 30mL solution of 4-NP (0.1mM) resulting in a deep yellow coloured solution. After that, 20mg PPY/PB was added to the deep yellow solution and stirred at ambient conditions. Then the samples were collected at different intervals of time and followed with centrifugation. The concentration of 4-NP was monitored by a UV-visible spectrophotometer. The decrease in absorption intensity at 400nm was used to determine the progress of the catalytic reduction reaction.

Conclusions

This study highlights the targeted design of the PB/PPY nanocomposite as an adsorbent and its optimization towards adsorptive attenuation of M.G dye and INH antibiotic as representative contaminants under environmentally viable conditions. Besides, it envisages a perpetual water treatment method in which the adsorbent effectively traps contaminant for its surface concentration and activation towards a faster catalytic transformation followed by visible light-mediated self-cleaning of adsorbent for further treatment cycles. As a modular case of synergistic adsorptive and catalytic transformation, nitrophenol adsorption by PPY/PB nanocomposite was utilized in its catalytic reduction to aminophenol using $NaBH_4$ as a reducing agent under dark conditions. The structure-activity response-based adsorption propensity of M.G dye and INH antibiotic towards PB/PPY was monitored for their corresponding adsorption capacities. The optimization of adsorption influencing factors (pH, temperature, initial contaminant concentration, adsorbent dose, contact time) was systematically conducted to customize the adsorptive avidity of contaminants under environmentally viable conditions. The thermodynamic studies indicated the adsorption process to be spontaneous and exothermic in nature. The equilibrium studies, and kinetic model fitting, aided with FTIR analysis, have been employed in the prediction of the adsorption mechanism. The mixed mechanism involving surface adsorption via physisorption, as well as the pore-filling effect as a plausible adsorption mechanism, can be proposed based on FTIR and control experiments. The major interactions involved in physisorption are pi-stacking, electrostatic, and hydrogen bonding type interactions. The surface concentration and activation of 4-NP adsorbate and surface generation of active hydrogen from $NaBH_4$ can be the plausible mechanism for the synergistic reduction of toxic 4-nitrophenol to less toxic 4-aminophenol.

Author Contributions

Prof. Masood Ahmad Rizvi and Prof. Jin Shang: conceptualization, design of the research work, resources, manuscript draft and review, editing, and overall supervision. Tabee Jan: experimental bench work, data curation, data analysis, hypothesis, and original manuscript draft. Shabnam Raheem: electrochemical methodology and hypothesis build-up, Aamir Hanif: spectral data analysis, draft write-up, manuscript editing. G.M. Peerzada data analysis editing the draft version and supervision. Prof. Gaulthier Rydzek and Prof. Katsuhiko Ariga: manuscript draft and review, editing.

Conflicts of interest

There are no conflicts to declare

Acknowledgments

Prof. Masood Ahmad Rizvi wishes to thank Professor G.R. Desiraju the Managing Trustee of CRYSTALLOGRAPHY IN INDIA Trust for the financial assistance towards restoration of scientific equipment used in this work. Prof. Masood Ahmad Rizvi also acknowledges DST, GOI for SURE Project grant SUR/2022/004046.

References

1 J.P.Obbard, Q.Q. Li, A. Loganath, Y.S. Chong, J. Tan and S. Bayen, Persistent Organic Pollutants and Adverse Health Effects in Humans in Singapore, Developments in Environmental Science,2007, 7 721-752.

2 P.E.Stackelberg,E.T.Furlong,M.T.Meyer,S.D.Zaugg, A.K. Henderson and D.B.Reissman, Persistence of pharmaceutical compounds and other organic wastewater contaminants in a conventional drinking-water-treatment plant, Sci. Total Environ.,2004,329, 99-113.

3 C.Pearce, J.Lloyd and J.Guthrie, The removal of colour from textile wastewater using whole bacterial cells: a review, Dyes Pigm.,2003, 58, 179-196.

4 M.Rafatullah,O.Sulaiman,R.Hashim and A.Ahmad,Adsorption of methylene blue on low-cost adsorbents: a review, J.Hazard. Mater.,2010, 177, 70-80.

5 M.A.Ahmad and R.Alrozi, Removal of malachite green dye from aqueous solution using rambutan peel-based activated carbon: Equilibrium, kinetic and thermodynamic studies, J.Chem.Eng.,2011,171, 510-516.

6 S.Srivastava, R.Sinha and D.Roy, Toxicological effects of malachite green, Aquat.Toxicol.,2004, 66, 319-329.

7 R.Coronado-Castañeda,M.Maya-Treviño,E.Garza-González,J.Peral,M.Villanueva-Rodríguez and A.Hernández-Ramírez, Photocatalytic degradation and toxicity reduction of isoniazid using β-Bi2O3 in real wastewater, Catal.Today,2020, 341, 82-89.

8 N.H.Tran,M.Reinhard and K.Y.-H.Gin, Occurrence and fate of emerging contaminants in municipal wastewater treatment plants from different geographical regions-a review, Water Res.,2018,133,182-207.

9 J.Bengtsson-Palme and D.J.Larsson, Concentrations of antibiotics predicted to select for resistant bacteria: proposed limits for environmental regulation, Environ. Int., 2016,86,140-149.

10 V.Mhuka,S.Dube and M.M.Nindi,Occurrence of pharmaceutical and personal care products (PPCPs) in wastewater and receiving

waters in South Africa using LC-Orbitrap™ MS, Emerg.Contam.,2020, 6, 250-258.

11 M. Beydaghdari, F.H. Saboor, A. Babapoor and M. Asgari, Recent progress in adsorptive removal of water pollutants by metal-organic frameworks, ChemNanoMat.,2022, 8, e202100400.

12 S.Guo, Y.Li, Y.Wang, L.Wang, Y.Sun and L.Liu, Recent advances in biochar-based adsorbents for CO2 capture, Carbon Capture Sci. Technol.2022, 100059.

13 C.Zhang, S.Sun, S.Xu and C.Wu, CO2 capture over steam and KOH activated biochar: Effect of relative humidity, Biomass Bioenergy,2022, 166 ,106608.

14 T.Wang, B.Tian, B.Han, D.Ma, M.Sun, A.Hanif, D.Xia and J.Shang, Recent advances on porous materials for synergetic adsorption and photocatalysis, Energy Environ. Mater.,2022,5,711-730.

15 A.Deronzier and J.-C.Moutet,Polypyrrole films containing metal complexes:syntheses and applications, Coord.Chem. Rev.,1996,147, 339-371

16 T.Wang, L.Yan, Y.He,S.I.Alhassan,H.Gang,B.Wu, L.Jin and H.Wang, Application of polypyrrole-based adsorbents in the removal of fluoride: a review, RSC Adv.,2022,12, 3505-3517.

17 Q.Xin, J.Fu, Z.Chen, S.Liu, Y.Yan, J.Zhang and Q.Xu, Polypyrrole nanofibers as a high-efficient adsorbent for the removal of methyl orange from aqueous solution, J.Environ.Chem.Eng.,2015, 3, 1637-1647.

18 F.Gao,X.Hou,A.Wang,G.Chu,W.Wu,J.Chen and H.Zou,Preparation of polypyrrole/TiO2 nanocomposites with enhanced photocatalytic performance, Particuology,2016, 26 ,73-78.

19 M.Rizvi, S.Akhoon, S.Maqsood and G.Peerzada, Synergistic effect of perchlorate ions and acetonitrile medium explored for extension in copper redoximetry, J.Anal. Chem.,2015, 70,633-638.

20 I.Yousuf, M.Zeeshan, F.Arjmand, M.A.Rizvi and S.Tabassum, Synthesis, structural investigations and DNA cleavage properties of a new water soluble Cu (II)–iminodiacetate complex, Inorg.Chem. Commun.,2019, 106 , 48-53.

21 M.A.Ganie, M.A.Rizvi, S.Raheem and B.A.Shah,Synthesis of 1,2-oxazetidines with a free–NH group via photoredox catalysis, ChemComm.,2022, 58, 8508-8511.

22 M.A.Rizvi, S.K.Moosvi, T.Jan, S.Bashir, P.Kumar,W. Roos and H.Swart, Dielectric, magnetic and photocatalytic activity of PolyPyrrole/Prussian red nanocomposite for waste water treatment applications, Polymer,2019, 163, 1-12.

23 M.Mustafa,S.Bashir,S.K.Moosvi,M.Najar,M.H.Masoodi and M.A.Rizvi, Hybrid Polymer Composite of Prussian Red Doped Polythiophene for Adsorptive Wastewater Treatment Application, Acta Chim.Slov.,2022,69.

24 H. Seema, N. Khan, A.ul H.A.Shah and A. Muhammad, Fabrication of self-assembled Prussian blue graphene hydrogel for highly selective removal of radioactive cesium in water: Adsorption study, Mater. Chem. Phys.,2023,306, , 128003.

25 Y.C. López, G. A. Ortega, M. A. Martínez and E. Reguera ,Magnetic Prussian Blue derivative like absorbent cages for an efficient thallium removal, J. Clean. Prod.,2021, 283, 124587.

26 T.Jan,M.A.Rizvi,S.K.Moosvi,M.H.Najar,S.H.Mir and G.M.Peerzada, A switching-type positive temperature coefficient behavior exhibited by PPy/(PhSe)2 nanocomposite prepared by chemical oxidative polymerization, ACS omega,2021, 6, 7413-7421.

27 M.Maruthapandi,A.P.Nagvenkar, I. Perelshtein, and A.Gedanken, Carbon-Dot Initiated Synthesis of Polypyrrole and Polypyrrole@CuO Micro/Nanoparticles with Enhanced Antibacterial Activity, ACS Appl. Polym. Mater., 2019, 1,1181–1186.

28 S.Muthusamy,J.Charles,B.Renganathan and D.Sastikumar,In situ growth of Prussian blue nanocubes on polypyrrole nanoparticles: facile synthesis, characterization and their application as fiber optic gas sensor, J. Mater. Sci.,2018, 53,15401-15417.

29 J.Allen and A.Bonnette Jr, Thermal decomposition of Prussian blue:Isotopic labeling with Mössbauer-inactive Fe-56, J.inorg. nucl. chem., 1974,36,1011-1016.

30 B.Boukoussa, F.Abidallah, Z.Abid, Z.Talha, N.Taybi, H. Sid El Hadj, R.Ghezini,R. Hamacha, A.Bengueddach, Synthesis of polypyrrole/Fe-kanemite nanocomposite through in situ polymerization: effect of iron exchange, acid treatment, and CO2 adsorption properties, J.Mater. Sci.,2017, 52, 2460-2472.

31 R.Ullah,N.Khan,R.Khattak,M.Khan,M.S.Khan and O.M.Ali, Preparation of electrochemical supercapacitor based on polypyrrole/gum arabic composites, Polym.,2022, 14,242.

32 W.Zheng, S.Li, X.Yu, C.Chen, H.Huang, Y.Huang and L.Li, Synthesis of hierarchical reduced graphene oxide/SnO2/polypyrrole ternary composites with high electrochemical performance, Mater. Res. Bull.,2016, 80, 303-308.

33 R.Swetha,M.U.Kumar and L.Kumari, Synthesis and characterization of polypyrrole-Ce0. 05CoSb3 nanocomposites,Mater.Today:Proc.,2021, 46, 2934-2939.

34 M.Fallahian,B.Pourabbas,M.Sharif, K.Froutani, M.Mahmoodian and M.Mohammadizadeh, Preparation of conductive,flexible and transparent films by in situ deposition of polypyrrole nanoparticles on polyethylene terephthalate, Polym.Sci.Ser.B,2017, 59, 308-319.

35 Z.Ryu, J.Zheng, M.Wang and B.Zhang,Characterization of pore size distributions on carbonaceous adsorbents by DFT, Carbon,1999, 37, 1257-1264.

36 Y.Li, Z.Li and P.K.Shen, Simultaneous formation of ultrahigh surface area and three-dimensional hierarchical porous graphene-like networks for fast and highly stable supercapacitors, Adv.Mater., 2013,25, 2474-2480.

37 M.Thommes, K.Kaneko,A.V.Neimark,J.P.Olivier,F.Rodriguez-Reinoso,J.Rouquerol and K.S.Sing, Physisorption of gases, with special reference to the evaluation of surface area and pore size distribution (IUPAC Technical Report), Pure Appl.Chem.,2015, 87, 1051-1069.

38 U.O.Aigbe,R.B.Onyancha,K.E.Ukhurebor and K.O.Obodo, Removal of fluoride ions using a polypyrrole magnetic nanocomposite influenced by a rotating magnetic field, RSC Adv.,2020,10 595-609.

39 L.Yan,W.Li, Q.Zhao, Z. Zhu, C. Hu and B. Liu, Enhanced photocatalytic conversion of (3D/2D) BiVO4@ Polypyrrole/g-C3N4 ternary composites with Z-scheme band alignment for the Antibiotic removal, Colloids Surf. A: Physicochem. Eng. Asp., 2021,624 ,126783.

40 K. Grace Pavithra, V.Jaikumar, P. S.l Kumar, P. Sundarrajan, Removal of emerging pollutants from aquatic system using electrochemical treatment and adsorption: Comparison and analysis, Environ. Technol. Innov.,23, 2021, 101754.

41 A. Ajith ,N. S. K. Gowthaman,S. A. John, and K. P. Elango,Direct Adsorption of Graphene Oxide on a Glassy Carbon Electrode: An Investigation of Its Adsorption and Electrochemical Activity, Langmuir 2023, 39, 29, 9990–10000

42 C.L.C.Carvalho, G.de Andrade Rodrigues, J.L. Magalhães, R.A. de Sousa Luz, E.T.S.G. da Silva andW.Cantanhêde, Effect of Ibuprofen on the electrochemical properties of Prussian blue/single-walled carbon nanotubes nanocomposite modified electrode, Surf. Interfaces,2021, 25 , 101276.

43 O.Makowski, J.Stroka, P.J.Kulesza, M.A.Malik and Z.Galus, Electrochemical identity of copper hexacyanoferrate in the solid-state: evidence for the presence and redox activity of both iron and copper ionic sites, J.Electroanal.Chem.,2002, 532,157-164.

44 G.Y. Abate, A.N. Alene, A.T. Habte and D.M. Getahun, Adsorptive removal of malachite green dye from aqueous solution onto activated carbon of Catha edulis stem as a low cost bio-adsorbent, Environ.Syst.Res.,2020, 9, 1-13.

45 Y.-C. Lee, J.-Y. Kim and H.-J. Shin, Removal of malachite green (MG) from aqueous solutions by adsorption, precipitation, and alkaline fading using talc, Sep Sci Technol., 2013,48 ,1093-1101.

46 A.S. Sartape, A.M. Mandhare, V.V.Jadhav, P.D.Raut, M.A.Anuse and S.S. Kolekar, Removal of malachite green dye from aqueous solution with adsorption technique using Limonia acidissima (wood apple) shell as low cost adsorbent, Arab.J.Chem., 2017,10, S3229-S3238.

47 E.Çalışkan Salihi and E.Aydın, Adsorptive characteristics of isoniazid on powdered activated carbon: π–π Dispersion interactions at the solid–solution interface, J.Dispers. Sci. Technol.,2017, 38, 457-462.

48 E.Çalışkan Salihi,Z.Gündüz and A.S.Baştuğ, Fast retention of isoniazid on organobentonite prepared using green chemistry approach:contribution of the π interactions, Sep.Sci.Technol.,2019,54 2695-2705.

49 C.Dube, R.Tandlich and B.Wilhelmi,Adsorptive removal of ciprofloxacin and isoniazid from aqueous solution, Nova Biotechnol.Chim.,2018, 17, 16-28.

50 A.Deb, A. Debnath, K. Bhowmik, S. R. Paul and B. Saha,Application of polyaniline impregnated mixed phase Fe2O3, MnFe2O4 and ZrO2 nanocomposite for rapid abatement of binary dyes from aqua matrix: response surface optimisation, J. Environ. Anal. Chem., 2023, 103, 5938–5956.

51 A. Deb ,A. Debnath,and B. Saha, Ultrasound-aided rapid and enhanced adsorption of anionic dyes from binary dye matrix onto novel hematite/polyaniline nanocomposite: Response surface methodology optimization, Appl Organometal Chem., 2019,34,e5353.

52 C.Li,H.Zhong,S.Wang,J.Xue and Z.Zhang, Removal of basic dye (methylene blue) from aqueous solution using zeolite synthesized from electrolytic manganese residue, J.Ind.Eng.Chem.,2015,23, 344-352.

53 G.Moussavi,S.Talebi,M.Farrokhi and R.M. Sabouti, The investigation of mechanism, kinetic and isotherm of ammonia and humic acid co-adsorption onto natural zeolite, J.Chem.Eng.,2011,171 1159-1169.

54 A.Mollahosseini,A.Khadir and J.Saeidian,Core–shell polypyrrole/Fe3O4 nanocomposite as sorbent for magnetic dispersive solid-phase extraction of Al+3 ions from solutions: investigation of the operational parameters, J.Water Process.Eng.,2019, 29 ,100795.

55 I.M.Kenawy,M.A.Hafez,A.A.Mousa, Z.A. Elbary and K.S. Abou-El-Sherbini, Removal of Isolan Dark Blue 2SGL-01 from aqueous solutions onto calcined and uncalcined (Mg-Zn)/(Al-Fe)-(CO 3)/Cl layered double hydroxides,Sustain.Environ.Res.,2021, 31, 1-14.

56 A.A.Alqadami,M.Naushad,Z.A.Alothman and A.A.Ghfar,Novel metal–organic framework (MOF) based composite material for the sequestration of U (VI) and Th (IV) metal ions from aqueous environment, ACS Appl.Mater.Interfaces,2017, 9, 36026-36037.

57 M.Zbair, Z.Anfar, H.A.Ahsaine and H.Khallok, Kinetics, equilibrium, statistical surface modeling and cost analysis of paraquat removal from aqueous solution using carbonated jujube seed, RSC Adv.,2019, 9, 1084-1094.

58 R.Soltani,A.Marjani and S.Shirazian,A hierarchical LDH/MOF nanocomposite:single, simultaneous and consecutive adsorption of a reactive dye and Cr (vi), Dalton Trans.,2020, 49, 5323-5335.

59 F.Mohamed, M.R.Abukhadra and M. Shaban, Removal of safranin dye from water using polypyrrole nanofiber/Zn-Fe layered double hydroxide nanocomposite (Ppy NF/Zn-Fe LDH) of enhanced adsorption and photocatalytic properties, Sci.Total Environ., 2018,640, 352-363.

60 S.Fan, Y.Wang, Z.Wang, J.Tang, J.Tang and X.Li, Removal of methylene blue from aqueous solution by sewage sludge-derived biochar: Adsorption kinetics, equilibrium, thermodynamics and mechanism, J.Environ.Chem.Eng., 2017,5, 601-611.

61 Y.Huang, C.Yang, Z.Sun, G.Zeng and H.He, Removal of cadmium and lead from aqueous solutions using nitrilotriacetic acid anhydride modified ligno-cellulosic material, RSC Adv.,2015, 5, 11475-11484.

62 J.Wang and X.Guo, Adsorption isotherm models: Classification, physical meaning, application and solving method, Chemosphere,2020, 258 , 127279.

63 A.L.Taka, E.Fosso-Kankeu, K.Pillay and X.Y.Mbianda, Removal of cobalt and lead ions from wastewater samples using an insoluble nanosponge biopolymer composite: adsorption isotherm, kinetic, thermodynamic, and regeneration studies, Environ. Sci. Pollut. Res.,2018,25, 21752-21767.

64 X.Tang, G.Ran, J.Li, Z.Zhang and C.Xiang, Extremely efficient and rapidly adsorb methylene blue using porous adsorbent prepared from waste paper: Kinetics and equilibrium studies, J.Hazard. Mater.,2021, 402 , 123579.

65 R.Haounati, H.Ouachtak, R. El Haouti, S.Akhouairi, F. Largo, F. Akbal, A. Benlhachemi, A. Jada and A.A.Addi, Elaboration and properties of a new SDS/CTAB@ Montmorillonite organoclay composite as a superb adsorbent for the removal of malachite

green from aqueous solutions, Sep. Purif. Technol.,2021, 255 , 117335.

66 H.U.R.Shah, K.Ahmad, H.A.Naseem,S.Parveen,M.Ashfaq,A.Rauf and T.Aziz, Water stable graphene oxide metal-organic frameworks composite (ZIF-67@ GO) for efficient removal of malachite green from water, Food Chem.Toxicol.,2021, 154 ,112312.

67 R. Soltani, A.Marjani, R.Soltani and S.Shirazian, Hierarchical multi-shell hollow micro–meso–macroporous silica for Cr (VI) adsorption, Sci.Rep.,2020, 10, 9788.

68 Bulin, T.Guo, R.Zheng, Q. Xiong,Interaction mechanism of phytic acid functionalized graphene oxide with ionic dyes, Sep. Purif. Technol.,2024, 330 , 125369.

69 M. Abbasi, M.M. Sabzehmeidani, M. Ghaedi, R. Jannesar and A.Shokrollahi, Synthesis of grass-like structured Mn-Fe layered double hydroxides/PES composite adsorptive membrane for removal of malachite green, Appl. Clay Sci.,2021, 203, 105946.

70 E.Çalışkan Salihi, J.Wang, G.Kabacaoğlu, S.Kırkulak and L.Šiller, Graphene oxide as a new generation adsorbent for the removal of antibiotics from waters, Sep Sci Technol., 2021,56, 453-461.

71 Y.Zeng, L.Zhao, W.Wu, G.Lu, F.Xu, Y.Tong, W.Liu and J.Du, Enhanced adsorption of malachite green onto carbon nanotube/polyaniline composites, J.Appl.Polym.Sci.,2013,127 , 2475-2482.

72 A.A.Khan, R.Ahmad, A.Khan and P.K.Mondal, Preparation of unsaturated polyester Ce (IV) phosphate by plastic waste bottles and its application for removal of Malachite green dye from water samples, Arab.J.Chem., 2013,6, 361-368.

73 V.Muinde, J.M.Onyari, B.M.Wamalwa and J.Wabomba, Adsorption of malachite green from aqueous solutions onto rice husks: kinetic and equilibrium studies, J. Environ. Prot.,2017, 8, 215.

74 V.M. Muinde, J.M. Onyari, B. Wamalwa and J.N. Wabomba, Adsorption of malachite green dye from aqueous solutions using mesoporous chitosan–zinc oxide composite material, J.Environ.Chem. Ecotoxicol., 2020,2 ,115-125.

75 M. Rajabi, B. Mirza, K. Mahanpoor, M. Mirjalili, F. Najafi, O. Moradi, H. Sadegh, R. Shahryari-Ghoshekandi, M. Asif and I.Tyagi, Adsorption of malachite green from aqueous solution by carboxylate group functionalized multi-walled carbon nanotubes: determination of equilibrium and kinetics parameters, J.Ind.Eng Chem.,2016, 34 , 130-138.

76 F.Nasiri Azad,M.Ghaedi,K.Dashtian,S.Hajati,A.Goudarzi and M.Jamshidi,Enhanced simultaneous removal of malachite green and safranin O by ZnO nanorod-loaded activated carbon: modeling, optimization and adsorption isotherms , New J. Chem.,2015, 39, 7998-8005.

77 T.A.Khan, R.Rahman, I.Ali, E.A.Khan and A.A.Mukhlif, Removal of malachite green from aqueous solution using waste pea shells as low-cost adsorbent adsorption isotherms and dynamics, Toxicol Environ Chem.,2014, 96 ,569–578.

78 Y.Fu, P.Xu, D.Huang, G.Zeng, C.Lai, L.Qin, B.Li, J.He, H.Yi and M.Cheng, Au nanoparticles decorated on activated coke via a facile preparation for efficient catalytic reduction of nitrophenols and azo dyes, Appl.Surf. Sci.,2019, 473 , 578-588.

79 T.Aditya, A.Pal and T.Pal, Nitroarene reduction: a trusted model reaction to test nanoparticle catalysts, ChemComm.,2015, 51, 9410-9431.

80 S.Ahmad, C.Yang, W.Xie, Z. Deng, H. Zhang, Y. Zhao and X.Su, Molten salt-templated synthesis of ternary NiS–NiCo2O4@ C composites as high performance catalysts for 4-nitro phenol reduction and supercapacitor, Carbon,2020, 158 ,912-921.

81 Z.D.Pozun, S.E.Rodenbusch, E.Keller, K.Tran, W.Tang, K.J.Stevenson and G.Henkelman, A systematic investigation of p-nitrophenol reduction by bimetallic dendrimer encapsulated nanoparticles, J.Phys.Chem.C, 2013,117,7598-7604.

82 R.He, B.Tang,C.Ton-That,M.Phillips and T.Tsuzuki, Physical structure and optical properties of Co-doped ZnO nanoparticles prepared by co-precipitation, J Nanopart Res.,2013,15, 1-8.

83 T.Jan,S.K.Moosvi,M.H.Najar,G.M.Peerzada and M.A.Rizvi, Diphenyldiselenide modulated charge transport dynamics,impedance spectroscopy and temperature sensing behaviour of polythiophene, J.Mater.Sci. Mater.,2022, 33, 8179-8192.

84 A. Deb, A. Debnath, N. Bhattacharjee and B. Saha,Ultrasonically enhanced dye removal usingconducting polymer functionalised ZnO nanocomposite at near neutral pH: kinetic study,isotherm modelling and adsorbent cost analysis J. Environ. Anal. Chem., 2022, 102, 8055–8074

85 I.Ali, C.Peng, T.Ye and I.Naz,Sorption of cationic malachite green dye on phytogenic magnetic nanoparticles functionalized by 3-marcaptopropanic acid, RSC Adv., 2018, 8, 8878-8897.

86 I.M.S.Souza, A B.-Sánchez, C.Ignacio Sainz-Díaz, C.Viseras,and S.B.C.Pergher,Study of Faujasite zeolite as a modified delivery carrier for isoniazid, Mater. Sci. Eng.C, 2021,118 ,111365.

87 R.Jin,S.Sun,Y.Yang,Y. Xing,D.Yu,X. Yu,and S.Song,Size-Dependent Catalytic Properties of Au Nanoparticles Supported on Hierarchical Nickel Silicate Nanostructures, Dalton Trans., 2013,42, 7888-7893.